

The MASSIVE Survey - VIII. Stellar Velocity Dispersion Profiles and Environmental Dependence of Early-Type Galaxies

Melanie Veale,^{1,2★} Chung-Pei Ma,^{1,2★} Jenny E. Greene,³ Jens Thomas,⁴

John P. Blakeslee,⁵ Jonelle L. Walsh,⁶ Jennifer Ito¹

¹*Department of Astronomy, University of California, Berkeley, CA 94720, USA*

²*Department of Physics, University of California, Berkeley, CA 94720, USA*

³*Department of Astrophysical Sciences, Princeton University, Princeton, NJ 08544, USA*

⁴*Max Planck-Institute for Extraterrestrial Physics, Giessenbachstr. 1, D-85741 Garching, Germany*

⁵*Dominion Astrophysical Observatory, NRC Herzberg Astronomy & Astrophysics, Victoria BC V9E2E7, Canada*

⁶*George P. and Cynthia Woods Mitchell Institute for Fundamental Physics and Astronomy, and Department of Physics and Astronomy, Texas A&M University, College Station, TX 77843, USA*

Accepted XXX. Received YYY; in original form ZZZ

ABSTRACT

We measure the radial profiles of the stellar velocity dispersions, $\sigma(R)$, for 90 early-type galaxies (ETGs) in the MASSIVE survey, a volume-limited integral-field spectroscopic (IFS) galaxy survey targeting all northern-sky ETGs with absolute K -band magnitude $M_K < -25.3$ mag, or stellar mass $M_* \gtrsim 4 \times 10^{11} M_\odot$, within 108 Mpc. Our wide-field $107'' \times 107''$ IFS data cover radii as large as 40 kpc, for which we quantify separately the inner (2 kpc) and outer (20 kpc) logarithmic slopes γ_{inner} and γ_{outer} of $\sigma(R)$. While γ_{inner} is mostly negative, of the 56 galaxies with sufficient radial coverage to determine γ_{outer} we find 36% to have rising outer dispersion profiles, 30% to be flat within the uncertainties, and 34% to be falling. The fraction of galaxies with rising outer profiles increases with M_* and in denser galaxy environment, with 10 of the 11 most massive galaxies in our sample having flat or rising dispersion profiles. The strongest environmental correlations are with local density and halo mass, but a weaker correlation with large-scale density also exists. The average γ_{outer} is similar for brightest group galaxies, satellites, and isolated galaxies in our sample. We find a clear positive correlation between the gradients of the outer dispersion profile and the gradients of the velocity kurtosis h_4 . Altogether, our kinematic results suggest that the increasing fraction of rising dispersion profiles in the most massive ETGs are caused (at least in part) by variations in the total mass profiles rather than in the velocity anisotropy alone.

Key words: galaxies: elliptical and lenticular, cD – galaxies: evolution – galaxies: formation – galaxies: kinematics and dynamics – galaxies: structure

1 INTRODUCTION

Measuring the stellar velocity dispersion profiles of elliptical galaxies is a key ingredient of estimating their dark matter content. However, unlike spiral galaxies in which ordered rotation allows a relatively straightforward translation of rotation curves into dark matter density profiles (e.g. Rubin et al. 1980), elliptical galaxies have a complex relationship between the gravitational potential, orbital configuration of

stars, and measured line-of-sight kinematics. In addition to the measurement of dark matter, details of these relationships can also shed light on the formation and assembly history of these galaxies.

Pre-1990 long-slit measurements of the stellar velocity dispersion profiles of elliptical galaxies found most of them to decline with radius out to ~ 10 kpc (Faber et al. 1977; Tonry 1985; Wilkinson et al. 1986; Davies & Illingworth 1986; Franx et al. 1989). There are a few notable exceptions. Faber et al. (1977) found the cD galaxy in Abell 401 to have a flat dispersion profile, measuring $\sigma \sim 480$ km s⁻¹ at two points (in the nucleus and at ~ 43 kpc). Davies & Illingworth (1983)

★ E-mail: melanie.veale@berkeley.edu (MV), cpma@berkeley.edu (C-PM)

found NGC 4889 and NGC 6909 to also have flat dispersion profiles out to ~ 10 kpc. Rising dispersion profiles were rare. Dressler (1979) found σ for IC 1101 (BCG of Abell 2029) to rise from 375 km s^{-1} at the center to 500 km s^{-1} at 70 kpc. Carter et al. (1981, 1985) found rising profiles for IC 2082 and the BCG of Abell 3266 (both double-nucleus galaxies) out to ~ 30 kpc, although data covering smaller radial ranges found falling or flat profiles (Tonry 1985).

Several long-slit studies since the 1990s have focused on brightest group or cluster galaxies (BGGs or BCGs), and again found mostly flat or falling dispersion profiles (Fisher et al. 1995; Sembach & Tonry 1996; Carter et al. 1999; Brough et al. 2007; Loubser et al. 2008). More than 60 galaxies were studied in these papers, but only four galaxies were found to have rising dispersion profiles. IC 1101 was confirmed as having a rising dispersion profile past at least 20 kpc (Fisher et al. 1995; Sembach & Tonry 1996). Carter et al. (1999) found NGC 6166 to have a rising profile at ~ 20 kpc, although observations with a smaller field of view found flat or falling profiles (Tonry 1985; Loubser et al. 2008). The rising profile of NGC 6166 has been confirmed in Kelson et al. (2002) and more recently in Bender et al. (2015), which found it to reach the cluster dispersion of 800 km s^{-1} at a radius of 50 kpc. This is the only study so far to confirm a smooth rise in dispersion in integrated starlight all the way to the cluster value. The dispersion profile of NGC 3311 starts to rise around 8 kpc and appears to extrapolate smoothly to the cluster dispersion (Hau et al. 2004), but the observations had a significant gap in radial coverage between the stellar dispersion and the cluster dispersion measured by galaxies. Loubser et al. (2008) and Ventimiglia et al. (2010) confirmed the rise in NGC 3311.

However, rising dispersion profiles may be more common than this, especially at large radius. Recently Newman et al. (2013) measured 7 more distant BCGs (redshifts 0.2 to 0.3) to about 30 kpc, and found all to be strikingly homogeneous in their rising dispersion profiles. Smith et al. (2017) also find a rising dispersion profile out to 30 kpc in the BCG of Abell 1201 at redshift 0.17. Globular cluster (GC) measurements have identified two other galaxies with rising dispersion profiles, NGC 1407 (Pota et al. 2015b) and NGC 4486 (M87; Cohen & Ryzhov 1997; Côté et al. 2001; Wu & Tremaine 2006), and confirmed the rising profile in NGC 3311 (Richtler et al. 2011). In the case of NGC 4486, looking at starlight, Sembach & Tonry (1996) found a falling profile, but Murphy et al. (2011, 2014) found a rise in σ at large radius. Other GC measurements of NGC 4486 found flat dispersion profiles to 200 kpc (Strader et al. 2011; Zhang et al. 2015; Ko et al. 2017), and GC measurements of several other galaxies in a similar mass range to MASSIVE have found flat and falling dispersion profiles (Côté et al. 2003; Schuberth et al. 2010; Richtler et al. 2014; Pota et al. 2013, 2015a). Inferring global population statistics from these heterogeneous results is made more difficult by the fact that different tracer populations (i.e. starlight and GCs) in general have different spatial distributions and orbital configurations, and thus different kinematics (e.g. Pota et al. 2013; Murphy et al. 2014).

Several past and ongoing IFU surveys produce 2-dimensional maps of stellar kinematics for large samples of galaxies and provide an even more comprehensive picture of velocity dispersion profiles than long-slit observations. The

ATLAS^{3D} survey (Emsellem et al. 2011) measured stellar kinematics to between $0.5R_e$ and $1R_e$ for a large sample of ETGs. Data beyond $1R_e$, however, are needed to study the outer behaviour of the dispersion profiles. The SLUGGS survey mapped the kinematics out to $\sim 3R_e$ for 25 ATLAS^{3D} galaxies (Brodie et al. 2014; Arnold et al. 2014). No dispersion profiles of these galaxies have been quantified thus far, but our visual inspections of their $\sigma(R)$ plots found only flat or falling dispersion profiles (Foster et al. 2016). Raskutti et al. (2014) measured kinematics to a few R_e for 33 ETGs and found flat or declining dispersion profiles past $1R_e$, with only the two most massive galaxies showing small increases in dispersion outside $1R_e$. The ongoing SAMI survey probes to between $1R_e$ and $2R_e$ (van de Sande et al. 2017) and may be more likely to provide statistics of the outer dispersion profiles.

A rising dispersion profile is generally interpreted as evidence for an increasing dynamical mass-to-light ratio, but velocity anisotropy can complicate the interpretations (Binney & Mamon 1982). Information about the full shape of the line-of-sight velocity distributions (LOSVD), in particular at least the kurtosis h_4 , is needed to determine both the mass and the anisotropy (Dejonghe & Merritt 1992; Merritt & Saha 1993; Gerhard 1993). Gravitational lensing data often favor roughly isothermal mass profiles for ETGs (Treu et al. 2006; Koopmans et al. 2009; Auger et al. 2009, 2010; Sonnenfeld et al. 2013). There is also some evidence that mass profiles depend on galaxy mass (Deason et al. 2012; Newman et al. 2013; Alabi et al. 2016) or environment (Newman et al. 2015), with steeper profiles at lower mass and density and shallower profiles at higher mass and density. If mass profiles change, then dispersion profiles are also likely to change with galaxy mass or environment. In addition, the anisotropy of a galaxy may be linked to its merger history (Romanowsky et al. 2003), which in turn links to galaxy mass and environment, and dispersion profiles may be directly impacted by recent mergers (Schauer et al. 2014).

In this paper we present the stellar velocity dispersion profiles, $\sigma(R)$, of 90 massive early-type galaxies in the volume-limited MASSIVE survey (Ma et al. 2014; Paper I). We measure the inner and outer gradients of $\sigma(R)$ and quantify how they correlate with galaxy mass, environment, and velocity kurtosis h_4 . The MASSIVE survey uses the wide-format ($107'' \times 107''$) Mitchell/VIRUS-P IFS to obtain 2-D kinematic maps out to radii as large as 40 kpc for the most massive local ETGs. The survey is designed with clean sample selection criteria, targeting all ETGs with stellar mass $M_* \gtrsim 4 \times 10^{11} M_\odot$ within 108 Mpc in the northern sky, regardless of galaxy environment, size, dispersion, or other properties. Details of our IFS data and kinematic analysis were described in Veale et al. (2017a) (Paper V). A study of the relationship between MASSIVE galaxy rotation, stellar mass, and four measures of galaxy environments (group membership, halo mass M_{halo} , large-scale galaxy density δ_g , and local galaxy density ν_{10}) was presented in Veale et al. (2017b) (Paper VII). This paper continues the stellar kinematic study of MASSIVE galaxies and focuses on the radial profiles of the stellar velocity dispersions.

Other results from the MASSIVE survey were discussed in separate papers: stellar population gradients (Greene et al. 2015; Paper II), molecular gas content and kinematics (Davis et al. 2016; Paper III), X-ray halo gas properties

(Goulding et al. 2016; Paper IV), spatial distributions and kinematics of warm ionized gas (Pandya et al. 2017; Paper VI), and measurement of the black hole mass in MASSIVE galaxy NGC 1600 (Thomas et al. 2016).

Section 2 of this paper summarizes our sample of galaxies and our earlier kinematic and environmental analyses. Section 3 describes how we quantify $\sigma(R)$ and presents our results for the inner and outer power law slopes γ_{inner} and γ_{outer} of $\sigma(R)$. Section 4 examines the relationships of the dispersion profiles and the higher moment h_4 , the kurtosis of the stellar velocity distribution, and Section 5 examines how the dispersion profiles relate to galaxy mass and environment. Section 6 summarizes the results and possible implications. The velocity dispersion profiles for all 90 galaxies are shown in Appendix A.

2 GALAXY SAMPLE, PROPERTIES, AND ENVIRONMENT

The MASSIVE survey targets a volume-limited sample of 116 early-type galaxies (ETGs) in the northern hemisphere and away from the galactic plane,¹ with stellar masses $M_* > 4 \times 10^{11} M_\odot$ (estimated from K -band magnitudes $M_K < -25.3$ mag) and distances $D < 108$ Mpc. The galaxies were selected from the Extended Source Catalogue (XSC; Jarrett et al. 2000) of the Two Micron All Sky Survey (2MASS; Skrutskie et al. 2006). The sample selection, methodology, and science goals of the survey were described in Ma et al. (2014) (Paper I of the MASSIVE survey). Uncertainties in galaxy parameters such as D , M_K , M_* , and R_e were discussed in Ma et al. (2014) and Veale et al. (2017a,b).

Thus far we have observed 90 MASSIVE galaxies with the Mitchell/VIRUS-P Integral Field Spectrograph (IFS) at the McDonald Observatory (Hill et al. 2008). This IFS covers a large $107'' \times 107''$ field of view with 246 evenly-spaced $4''$ -diameter fibres and a one-third filling factor, which we use to obtain contiguous coverage by observing each galaxy with three dither positions. The spectral range of the IFS spans 3650\AA to 5850\AA , covering the Ca H+K region, the G-band region, H β , the Mgb region, and many Fe absorption features. The instrumental resolution varies by factors of about 20 per cent over this wavelength range but is typically around 4.5\AA full width at half-maximum.

The spectra from individual fibres in the central regions of our galaxies typically have a signal-to-noise ratio (S/N) exceeding 50, and we use these single-fibre spectra directly in the kinematic analysis. Beyond the central regions, we combine the fibres with lower S/N into radial and azimuthal bins, folding across the major axis and combining symmetrical bins such that each resulting co-added spectrum reaches at least $S/N = 20$. The line-of-sight velocity distribution (LOSVD) is parametrized as a Gauss-Hermite series up to order 6, and we obtain the best-fitting velocity V , dispersion σ , and higher order moments h_3 , h_4 , h_5 , and h_6 using the penalized pixel-fitting (pPXF) method of Cappellari & Emsellem (2004). Details of our kinematic analysis such as spectral continuum modeling, stellar template fitting, and

error determination were described in Veale et al. (2017a) (Paper V).

Our results for four measures of galaxy environments – group membership, halo mass M_{halo} , large-scale galaxy density δ_g , and local galaxy density ν_{10} – were presented in Veale et al. (2017b) (Paper VII) and listed in Table 1. Briefly, we take group membership and halo mass information from the HDC catalogue of Crook et al. (2007, 2008), which is based on the 2MRS sample of Huchra et al. (2005a,b). Based on whether a galaxy is in a group with at least 3 members in the HDC catalogue, we assign each of our galaxies to be “Isolated”, a “Satellite” galaxy in a group, or “Brightest Group Galaxy” (BGG). Classification as a BGG is based entirely on the K -band luminosity, and is not necessarily equivalent to being the central galaxy (e.g. Skibba et al. 2011; Hoshino et al. 2015), and also does not distinguish cases where two galaxies are nearly matched in luminosity. We use M_{halo} measured by the projected mass estimator (Heisler et al. 1985) from the HDC catalogue; the 15 isolated galaxies in our sample therefore do not have a halo mass estimate. For the well-studied clusters of Virgo, Coma, and Perseus, we replace the M_{halo} taken from the HDC catalogue with values from the literature: $M_{\text{halo}} = 5.5 \times 10^{14} M_\odot$ for Virgo (Durrell et al. 2014; Ferrarese et al. 2012; Schindler et al. 1999), $M_{\text{halo}} = 1.8 \times 10^{15} M_\odot$ for Coma (Kubo et al. 2007; Falco et al. 2014; Rines et al. 2003), and $M_{\text{halo}} = 6.7 \times 10^{14} M_\odot$ for Perseus. The luminosity-weighted large-scale density contrast δ_g is calculated with a smoothing scale of a few Mpc in Carrick et al. (2015) based on the 2M++ redshift catalogue of Lavaux & Hudson (2011). We define the local density ν_{10} as the luminosity density within a sphere out to the 10th nearest neighbour of the galaxy, based on a parent catalogue including all galaxies with $M_K < -23.0$ from the 2MASS Redshift Survey (Huchra et al. 2012). With that luminosity cut, the parent catalogue is nearly (but not entirely) complete over our survey volume; see Section 3.4 and Appendix A of Veale et al. (2017b) for details.

3 RADIAL PROFILES OF STELLAR VELOCITY DISPERSION

3.1 Quantifying $\sigma(R)$

The radial profiles of the stellar velocity dispersion, $\sigma(R)$, for the 90 MASSIVE galaxies are shown in Figure 1 in three increasing M_* bins. As M_* increases (from left to right panels), the overall amplitude of σ increases, and more σ profiles become flat or rising in the outer parts instead of falling monotonically.

To quantify the overall shape of $\sigma(R)$, we fit a broken power law form as in Veale et al. (2017a):

$$\sigma(R) = \sigma_0 2^{\gamma_1 - \gamma_2} \left(\frac{R}{R_b} \right)^{\gamma_1} \left(1 + \frac{R}{R_b} \right)^{\gamma_2 - \gamma_1}, \quad (1)$$

where the break radius R_b is fixed at 5 kpc. Although the apparent break radius varies somewhat below and above this value among different galaxies, degeneracies among R_b , γ_1 , and γ_2 allow as good a fit for every galaxy with this fixed R_b as with a free R_b . Example fits are shown in Figure 2, and fits for all 90 galaxies are shown in Appendix A.

The parameters γ_1 and γ_2 in Equation 1 represent the asymptotic logarithmic slopes of $\sigma(R)$, whose values can be

¹ The total is 115 galaxies after we remove NGC 7681, which our IFS data revealed as a close pair of less-luminous bulges (Veale et al. 2017a), each below the magnitude cut of our survey.

Table 1. Properties of MASSIVE galaxies

Galaxy	M_K [mag]	$\log_{10} M_*$ [M_\odot]	λ_e	σ_c [km/s]	$\langle\sigma\rangle_e$ [km/s]	γ_{inner}	γ_{outer}	$\langle h_4 \rangle$	h'_4	env	$\log_{10} M_{\text{halo}}$ [M_\odot]	$1 + \delta_g$	v_{10} [\bar{v}]
(1)	(2)	(3)	(4)	(5)	(6)	(7)	(8)	(9)	(10)	(11)	(12)	(13)	(14)
NGC 0057	-25.75	11.79	0.022	289	251	-0.150	-0.001	0.053	0.017	I		2.29	4.8
NGC 0080	-25.66	11.75	0.039	248	222	-0.073	0.145	0.039	0.010	B	14.1	2.95	6500
NGC 0315	-26.30	12.03	0.062	348	341	-0.004	-0.057	0.052	0.011	B	13.5	6.03	270
NGC 0383	-25.81	11.82	0.252	290	257	-0.143	0.307	0.012	-0.019	S	14.4	7.24	4300
NGC 0410	-25.90	11.86	0.034	291	247	-0.121	-0.276	0.041	-0.028	B	14.4	7.41	3100
NGC 0499	-25.50	11.68	0.060	274	266	-0.043	-0.489	0.028	-0.008	S	14.4	7.24	35000
NGC 0507	-25.93	11.87	0.049	274	257	-0.069	(0.098)	0.050	0.035	B	14.4	7.24	58000
NGC 0533	-26.05	11.92	0.034	280	258	-0.056	0.068	0.063	0.083	B	13.5	4.27	13
NGC 0545	-25.83	11.83	0.129	249	231	0.011	(0.266)	0.074	0.036	B(A194)	14.5	5.89	13000
NGC 0547	-25.83	11.83	0.056	259	232	-0.079	(-0.006)	0.035	0.030	S(A194)	14.5	5.89	14000
NGC 0665	-25.51	11.68	0.402	206	164	-0.163	-0.070	-0.074	-0.227	B	13.7	3.02	56
UGC 01332	-25.57	11.71	0.037	248	253	-0.005	(0.274)	0.034	-0.020	B	13.8	3.72	170
NGC 0708	-25.65	11.75	0.036	206	219	-0.010	0.273	0.090	0.110	B(A262)	14.5	5.75	12000
NGC 0741	-26.06	11.93	0.040	292	289	0.012	(0.068)	0.043	0.069	B	13.8	2.88	130
NGC 0777	-25.94	11.87	0.046	324	291	-0.134	(-0.090)	0.051	0.004	B	13.5	5.01	76
NGC 0890	-25.50	11.68	0.101	207	194	-0.034	(-0.062)	-0.006	-0.002	I		4.68	1.4
NGC 0910	-25.33	11.61	0.039	236	219	-0.178	0.357	0.018	0.034	S(A347)	14.8	6.17	11000
NGC 0997	-25.40	11.64	0.243	267	215	-0.195	(-0.090)	0.021	-0.015	B	13.0	2.95	26
NGC 1016	-26.33	12.05	0.033	286	279	-0.028	-0.005	0.027	-0.001	B	13.9	4.79	55
NGC 1060	-26.00	11.90	0.023	310	271	-0.100	(-0.068)	0.055	0.028	B	14.0	3.89	2000
NGC 1132	-25.70	11.77	0.061	239	218	-0.100	0.145	0.022	0.015	B	13.6	3.39	8.1
NGC 1129	-26.14	11.96	0.120	241	259	0.036	0.131	0.047	0.043	B	14.8	10.72	16000
NGC 1167	-25.64	11.74	0.427	188	172	-0.085	-0.427	-0.068	-0.166	B	13.1	5.01	15
NGC 1226	-25.51	11.68	0.033	274	229	-0.146	-0.173	0.084	0.138	B	13.2	3.47	3.0
IC0 310	-25.35	11.61	0.085	218	205	-0.097	-	0.059	-0.074	S(Perseus)	14.8	13.18	15000
NGC 1272	-25.80	11.81	0.023	285	250	-0.075	0.118	0.049	0.046	S(Perseus)	14.8	13.49	39000
UGC 02783	-25.44	11.65	0.068	292	266	-0.163	(-0.143)	0.018	0.015	B	12.6	6.31	17
NGC 1453	-25.67	11.75	0.201	312	272	-0.091	0.013	0.044	0.005	B	13.9	2.29	87
NGC 1497	-25.31	11.60	0.474	234	190	-0.214	0.132	-0.029	-0.071	I		2.69	87
NGC 1600	-25.99	11.90	0.026	346	293	-0.082	-0.047	0.055	0.037	B	14.2	6.03	1200
NGC 1573	-25.55	11.70	0.040	288	264	-0.073	-0.254	0.018	0.015	B	14.1	4.07	580
NGC 1684	-25.34	11.61	0.122	295	262	-0.054	(-0.054)	0.018	0.011	B	13.7	6.17	1500
NGC 1700	-25.60	11.72	0.195	236	223	-0.086	-0.345	-0.026	-0.074	B	12.7	3.47	23
NGC 2208	-25.63	11.74	0.062	268	255	-0.024	(0.049)	-0.004	-0.007	I		2.82	7.1
NGC 2256	-25.87	11.84	0.024	240	259	0.121	(-0.103)	0.063	0.004	B	13.7	2.69	20
NGC 2274	-25.69	11.76	0.067	288	259	-0.083	0.133	0.021	-0.024	B	13.3	3.09	110
NGC 2258	-25.66	11.75	0.036	293	254	-0.080	(0.035)	0.040	0.042	B	12.2	3.80	9.5
NGC 2320	-25.93	11.87	0.235	340	298	-0.167	(0.000)	0.037	0.028	B	14.2	7.94	650
UGC 03683	-25.52	11.69	0.090	257	257	-0.051	(-0.093)	0.024	-0.090	B	13.6	5.75	26
NGC 2332	-25.39	11.63	0.037	254	224	-0.121	-0.123	0.029	-0.033	S	14.2	7.76	1500
NGC 2340	-25.90	11.86	0.029	232	235	-0.028	0.033	0.018	0.004	S	14.2	7.76	1200
UGC 03894	-25.58	11.72	0.122	297	255	-0.142	-0.107	0.036	0.025	B	13.7	1.55	1.5
NGC 2418	-25.42	11.64	0.241	245	217	-0.176	(-0.236)	0.041	-0.029	I		2.24	1.4
NGC 2513	-25.52	11.69	0.095	280	253	-0.071	-0.127	-0.004	-0.025	B	13.6	2.34	5.1
NGC 2672	-25.60	11.72	0.095	273	262	-0.055	(-0.033)	0.028	-0.009	B	13.0	1.32	1.2
NGC 2693	-25.76	11.79	0.295	327	296	-0.061	0.087	0.035	-0.011	I		1.70	6.8
NGC 2783	-25.72	11.78	0.042	252	264	0.034	0.012	0.047	-0.007	B	12.8	3.24	4.6
NGC 2832	-26.42	12.08	0.071	327	291	-0.093	0.096	0.054	0.005	B(A779)	13.7	3.98	7.8
NGC 2892	-25.70	11.77	0.046	237	234	0.013	-0.154	0.051	0.004	I		2.19	2.2
NGC 3158	-26.28	12.02	0.255	301	289	-0.034	0.009	0.032	0.009	B	13.3	2.69	9.5
NGC 3209	-25.55	11.70	0.039	288	247	-0.146	(-0.018)	0.005	-0.025	B	11.8	2.40	2.7
NGC 3462	-25.62	11.73	0.085	233	214	-0.048	-0.326	-0.017	-0.015	I		2.24	2.5
NGC 3562	-25.65	11.75	0.038	250	241	-0.069	-0.140	0.028	-0.021	B	13.5	2.24	8.3
NGC 3615	-25.58	11.72	0.399	268	232	-0.232	0.114	-0.030	-0.044	B	13.6	3.09	5.1
NGC 3805	-25.69	11.76	0.496	266	225	-0.262	0.086	0.019	-0.060	S(A1367)	14.8	5.62	430
NGC 3816	-25.40	11.64	0.105	212	191	-0.016	-0.142	-0.038	-0.055	S(A1367)	14.8	5.75	1900
NGC 3842	-25.91	11.86	0.038	262	231	-0.098	(0.046)	0.022	-0.000	B(A1367)	14.8	5.89	18000
NGC 3862	-25.50	11.68	0.045	248	228	-0.069	0.105	-0.005	-0.068	S(A1367)	14.8	5.89	18000
NGC 3937	-25.62	11.73	0.074	292	243	-0.150	(0.042)	0.015	-0.002	B	14.2	5.89	69
NGC 4073	-26.33	12.05	0.023	316	292	-0.101	0.199	0.034	0.043	B	13.9	4.37	87
NGC 4472	-25.72	11.78	0.197	292	258	-0.074	(-0.088)	0.023	0.020	B(Virgo)	14.7	8.91	1800
NGC 4555	-25.92	11.86	0.120	328	277	-0.097	-0.366	0.044	0.022	I		5.89	6.2
NGC 4816	-25.33	11.61	0.069	217	207	-0.031	-0.017	0.003	0.002	S(Coma)	15.3	13.18	1900

Table 1 – continued

Galaxy	M_K	$\log_{10} M_*$	λ_e	σ_c	$\langle\sigma\rangle_e$	γ_{inner}	γ_{outer}	$\langle h_4 \rangle$	h'_4	env	$\log_{10} M_{\text{halo}}$	$1 + \delta_g$	ν_{10}
(1)	[mag]	[M_{\odot}]	(4)	[km/s]	[km/s]	(7)	(8)	(9)	(10)	(11)	[M_{\odot}]	(13)	[\bar{v}]
NGC 4839	-25.85	11.83	0.053	261	275	-0.026	(0.298)	0.061	0.099	S(Coma)	15.3	13.18	2600
NGC 4874	-26.18	11.98	0.070	251	258	-0.030	0.255	0.046	0.051	S(Coma)	15.3	13.18	23000
NGC 4889	-26.64	12.18	0.032	370	337	-0.128	0.087	0.051	0.055	B(Coma)	15.3	13.18	18000
NGC 4914	-25.72	11.78	0.054	233	225	-0.023	-0.213	0.005	-0.032	I		1.12	1.1
NGC 5129	-25.92	11.86	0.402	260	222	-0.172	0.203	0.024	0.029	I		4.27	4.8
NGC 5208	-25.61	11.73	0.615	270	235	-0.226	(0.467)	0.001	-0.024	B	13.0	5.01	15
NGC 5322	-25.51	11.68	0.054	246	239	-0.073	(-0.178)	-0.002	-0.031	B	13.7	2.45	20
NGC 5353	-25.45	11.66	0.551	277	225	-0.141	(0.277)	0.018	-0.037	B	13.6	2.63	62
NGC 5490	-25.57	11.71	0.138	349	282	-0.272	(0.345)	0.056	0.020	I		2.14	9.5
NGC 5557	-25.46	11.66	0.035	279	223	-0.153	(0.120)	0.015	-0.056	B	13.3	2.57	8.3
NGC 6223	-25.59	11.72	0.315	274	238	-0.127	(-0.304)	0.008	0.006	B	13.5	1.55	6.0
NGC 6375	-25.53	11.69	0.240	226	187	-0.128	(-0.119)	0.021	-0.042	I		1.17	1.5
UGC 10918	-25.75	11.79	0.034	247	249	-0.121	0.185	0.018	0.051	I		1.78	4.7
NGC 6482	-25.60	11.72	0.137	305	291	-0.066	-0.174	0.009	-0.033	B	13.1	1.58	1.0
NGC 6575	-25.58	11.72	0.124	264	234	-0.098	(-0.156)	-0.011	-0.000	I		2.09	4.9
NGC 7052	-25.67	11.75	0.148	298	266	-0.093	-0.199	0.045	0.017	I		1.32	0.8
NGC 7242	-26.34	12.05	0.037	255	283	0.020	0.118	0.043	0.031	B	14.0	6.31	2700
NGC 7265	-25.93	11.87	0.039	230	206	-0.112	-0.034	-0.003	-0.061	B	14.7	6.92	5100
NGC 7274	-25.39	11.63	0.090	259	244	-0.089	0.230	0.030	0.003	S	14.7	6.92	3200
NGC 7386	-25.58	11.72	0.071	312	273	-0.071	-0.009	0.031	-0.003	B	13.9	2.57	3.1
NGC 7426	-25.74	11.79	0.563	284	219	-0.345	0.099	0.031	-0.048	B	13.8	3.80	8.3
NGC 7436	-26.16	11.97	0.085	280	263	-0.092	0.251	0.043	0.022	B	14.4	4.07	100
NGC 7550	-25.43	11.65	0.038	270	224	-0.117	-0.373	0.005	-0.030	B	11.9	0.93	1.0
NGC 7556	-25.83	11.83	0.049	253	243	-0.013	0.093	0.029	0.049	B	14.0	2.00	17
NGC 7618	-25.44	11.65	0.247	292	265	-0.127	-0.140	0.022	-0.014	B	13.7	3.16	240
NGC 7619	-25.65	11.75	0.119	325	277	-0.155	(0.073)	0.020	-0.002	B	14.0	1.55	21
NGC 7626	-25.65	11.75	0.034	269	250	-0.042	(-0.416)	0.045	-0.019	S	14.0	1.55	21

Column notes: (1) Galaxy name, in order of increasing right ascension (not listed) for consistency with previous MASSIVE papers. (2) Extinction-corrected 2MASS total absolute K -band magnitude. (3) Stellar mass estimated from M_K (eq. 2 of Ma et al. 2014, from Cappellari 2013). (4) Spin parameter λ within R_e . (5) Central fiber dispersion. (6) Average luminosity-weighted dispersion within R_e . (7) Power law slope of $\sigma(R)$ at 2 kpc. (8) Power law slope of $\sigma(R)$ at 20 kpc. When $R_{\text{max}} < 20$ kpc, the power law slope at R_{max} is listed instead, in parentheses. IC 0310 is removed from the list of outer fits entirely (see text). (9) Average luminosity-weighted h_4 within R_e , with typical formal errors ~ 0.01 . (10) Gradient in h_4 , defined as $\Delta h_4 / \Delta \log_{10} R$. (11) Group membership according to the 2MRS HDC catalogue: "B" for BGGs, "S" for satellites, "I" for isolated galaxies with fewer than 3 group members. Membership in Virgo, Coma, Perseus, or Abell clusters is listed. (12) Halo mass according to the HDC catalogue, or from updated literature sources (see text) for Virgo, Coma, and Perseus. (13) Large-scale galaxy overdensity from the 2M++ catalogue. (14) Local density in units of the mean K -band luminosity density $\bar{\nu} \sim 2.8 \times 10^8 L_{\odot} \text{Mpc}^{-3}$. (**) Additional columns will be included in the electronic version of the table, available as online supplementary material, including $\sigma(R)$ fit parameters γ_1 , γ_2 , and σ_0 and uncertainties on γ_{inner} and γ_{outer} .

more extreme than the slopes of $\sigma(R)$ in the radial range covered by our IFS data. To account for this, we convert γ_1 and γ_2 to the local logarithmic slopes γ_{inner} and γ_{outer} , where γ_{inner} is the power law slope of the fit at 2 kpc, and γ_{outer} is the power law slope of the fit at 20 kpc. We quote γ_{outer} only for the 56 galaxies ($\sim 2/3$ of the sample) where our data reach at least 20 kpc.²

Values of σ (and error bars) come directly from the analysis of Veale et al. 2017a (Paper V). The radial coordinates for each bin are a luminosity-weighted average over the radial coordinates of the fibre centres. For a single fiber near the centre of the galaxy, this can be quite inaccurate; a fibre of finite size with uniform flux that is exactly centred on the galaxy has an average radius of $2/3$ the fibre radius, not 0. We adjust the radial coordinates of our data to account for this effect, assuming uniform flux across each

fibre, and set the error on R to $0.5''$ to account for astrometric uncertainty. These adjustments avoid potential problems with the fits due to steep power laws being very sensitive at small radius.

Figure 2 illustrates three typical of $\sigma(R)$ shapes that we have found for MASSIVE galaxies: about 30% are consistent with a single power law ($\gamma_{\text{inner}} = \gamma_{\text{outer}}$, left panel), 50% have $\gamma_{\text{inner}} < \gamma_{\text{outer}}$ and typically fall to a minimum before rising at larger R (middle panel), and 20% have $\gamma_{\text{inner}} > \gamma_{\text{outer}}$ and are typically flat in the inner region then fall steeply at large R (right panel). Several galaxies in the last category are somewhat poor fits to the data in the very outskirts, with the fit declining more steeply than the data, but for the sake of uniformity we do not adjust the fits for these few galaxies. Instead, we simply note that the most negative values of γ_{outer} in our sample belong to these galaxies, and are likely over-estimating the steepness of the decline at the edges of our data.

Table 1 lists our measurements of γ_{inner} for all 90 MASSIVE galaxies and γ_{outer} for the 56 galaxies with a suffi-

² We also remove γ_{outer} for IC 0310, because it has unusually low σ in the outer bins and is a significant outlier with $\gamma_{\text{outer}} \sim -0.7$.

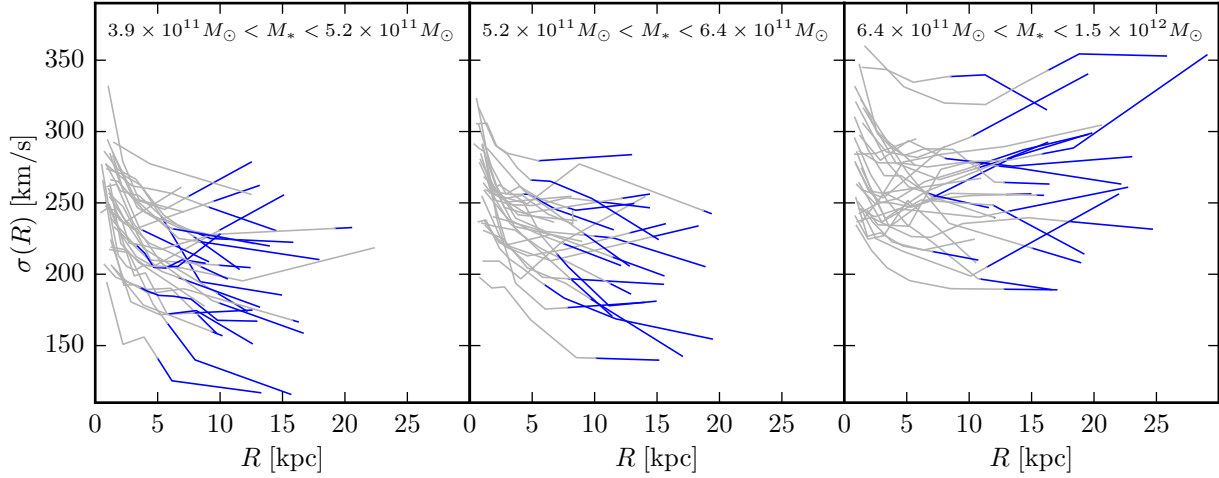


Figure 1. Stellar velocity dispersion profiles of 90 MASSIVE galaxies, calculated as a luminosity-weighted average of individual data points in each annulus. The 3 panels are arranged from low to high M_* , in equal-number bins corresponding to $-25.31 \text{ mag} > M_K > -25.60 \text{ mag}$ (left), $-25.60 \text{ mag} > M_K > -25.82 \text{ mag}$ (center), and $-25.82 \text{ mag} > M_K > -26.64 \text{ mag}$ (right). Each profile is blue at $R > R_e$, and the outermost point represents the *average* radius of the outermost bin; the total radial extent of the data is up to $\sim 60\%$ larger. From left to right, the overall amplitude of σ increases, with more profiles rising and fewer steeply falling.

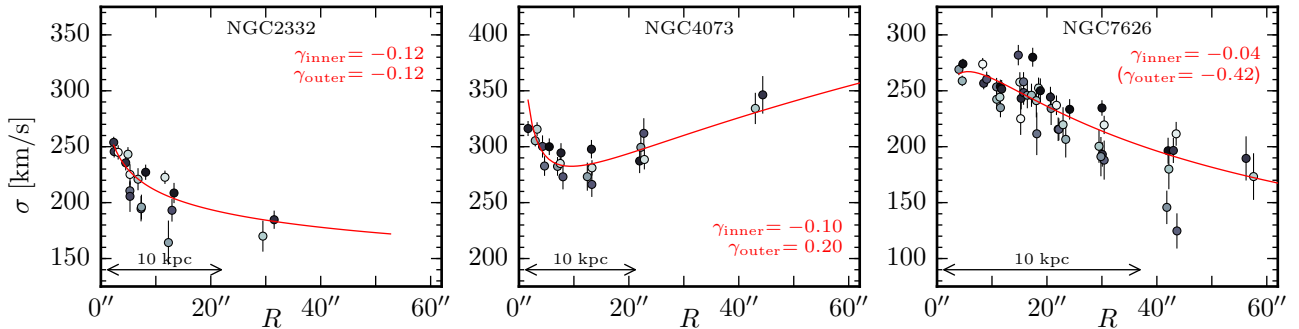


Figure 2. Examples of velocity dispersion profiles, with individual data points (black and white points near positive and negative major axis respectively, grey points near minor axis) and profile fits (red). About 30% of galaxies are fully consistent with a single power law fit (left panel), with 50% having $\gamma_{\text{outer}} > \gamma_{\text{inner}}$ (middle panel) and 20% having $\gamma_{\text{outer}} < \gamma_{\text{inner}}$. Most galaxies in the last category, by eye, appear to have a break radius smaller than the fiducial 5 kpc, and are often somewhat poor fits to the very outer data points (with the fit declining more steeply than the data). A compilation of this figure for all galaxies is shown in [Appendix A](#). Galaxies where $R_{\text{max}} < 20 \text{ kpc}$ have γ_{outer} measured at R_{max} (in parentheses) and are excluded from any statistics on γ_{outer} .

ciently large radial extent. [Figure 3](#) shows γ_{inner} versus γ_{outer} for these 56 galaxies. We define rising, flat, and falling outer profiles to be those with $\gamma_{\text{outer}} > 0$, $\gamma_{\text{outer}} = 0$ within errors, and $\gamma_{\text{outer}} < 0$ respectively. The sample is split nearly equally among the three types, with 36% rising, 30% flat, and 34% falling.

Uncertainties on γ_{inner} and γ_{outer} depend both on the uncertainty on the observed σ , and on whether the dispersion profile contains bumps, wiggles, or other features not accounted for in this simple fit. Errors range from 0.01 to 0.2, with typical errors of around 0.05. Errors for each galaxy are not tabulated in [Table 1](#) but will be available in the electronic version of the table. Flattened and/or fast rotating galaxies (e.g. NGC 5353) sometimes have a large spread in σ at large radius, and localized bumps in σ may be caused by the remains of merger activity ([Schauer et al. 2014](#)). Although mergers for very massive galaxies are expected to

be fairly common (e.g. [Edwards & Patton 2012](#); [Burke & Collins 2013](#)), galaxies with obvious interactions were removed in the original sample selection ([Ma et al. 2014](#)) so we expect the overall impact of mergers to be relatively minor. Some of the galaxies with $\gamma_{\text{inner}} > \gamma_{\text{outer}}$ might also be better fit by adding a second break radius, so that the center, intermediate radii, and outskirts could be fit by three distinct power laws. Our main goal is to quantify the statistics of overall $\sigma(R)$ behavior in a uniform way across our sample, so we do not address these features further here.

3.2 Effects of rotation: σ versus v_{rms}

Although many galaxies in the MASSIVE survey are slow or non-rotators ([Veale et al. 2017a,b](#)), 19 galaxies in the sample reported in this paper have spin parameter $\lambda_e \geq 0.2$ (see column 4 of [Table 1](#)), where the galaxy rotation V can

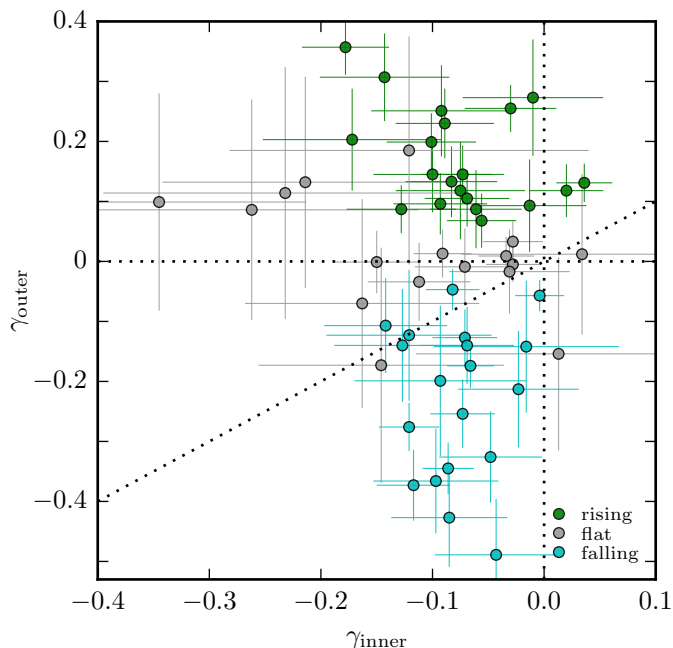


Figure 3. Outer vs. inner logarithmic slopes of $\sigma(R)$ for the 56 galaxies with binned data extending to at least 20 kpc. Most γ_{inner} are negative, while γ_{outer} spans a range of both positive and negative values. We classify galaxies by their outer profile behavior: rising (green), falling (cyan), or flat (gray), where any galaxy consistent with $\gamma_{\text{outer}} = 0$ (within errors) is considered flat. Galaxies with the most negative γ_{outer} tend to resemble NGC 1700 (right panel of Figure 2), where the fit likely over-estimates the steepness of the profile decline, but they are correctly identified as having a falling outer $\sigma(R)$ profile. Several galaxies are consistent with a single power law, $\gamma_{\text{inner}} = \gamma_{\text{outer}}$ (dotted line).

contribute a non-negligible amount to the second velocity moment $v_{\text{rms}} \equiv \sqrt{V^2 + \sigma^2}$.

To quantify the effects of rotation, we re-calculate γ_{outer} using $v_{\text{rms}}(R)$ instead of $\sigma(R)$ and compare the two slopes in Figure 4. As expected, the effect of rotation is to make the slopes of the v_{rms} profile less extreme than those of the σ profile. The changes in γ_{outer} due to the difference in v_{rms} and σ , however, are generally small and affect less than 20% of the sample.

Because the differences in slopes and profile fits between $v_{\text{rms}}(R)$ and $\sigma(R)$ are generally small and do not impact our results presented below, we will use $\sigma(R)$ and the slopes computed from $\sigma(R)$ for the rest of the paper.

3.3 The importance of a large field of view

Our IFS data extend up to 40 kpc, with most galaxies in the 15–30 kpc range, corresponding to ~ 1 to $4R_e$. This is usually far enough to capture the transition from falling inner σ to rising outer σ in U-shaped galaxies, but a galaxy identified as U-shaped with data out to 30 kpc would likely appear to be monotonically decreasing if viewed to less than 10 kpc.

Figure 5 shows how the outer profile behaviour γ_{outer} relates to the outer boundary of our IFS data R_{max} . Indeed, we find that galaxies with $R_{\text{max}} < 20$ kpc are less likely to

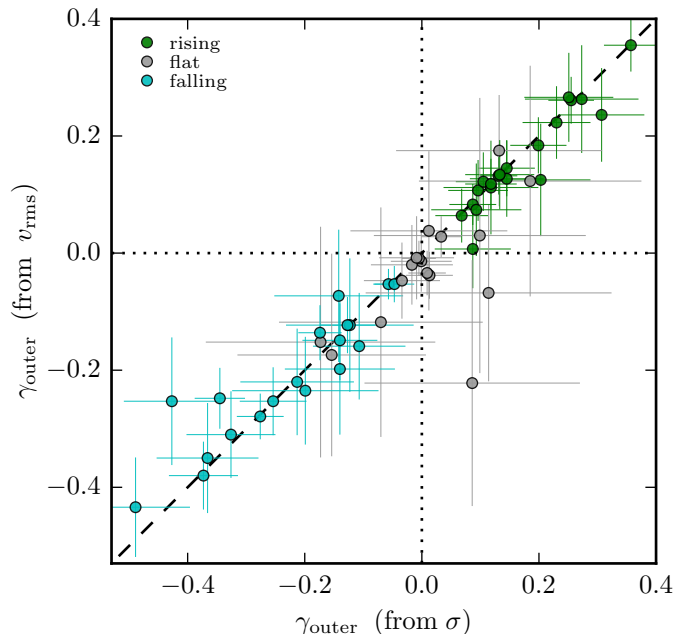


Figure 4. Comparison of γ_{outer} for $v_{\text{rms}}(R)$ and $\sigma(R)$. As expected, because v_{rms} is larger than σ for outer bins of fast rotators, the outer profile of $v_{\text{rms}}(R)$ is flatter than $\sigma(R)$ for a handful of galaxies. However, the difference in γ_{outer} is small overall since most galaxies in our sample are slow or non-rotators.

have rising outer profiles, and many of those with the smallest R_{max} have very few data points and uncertain fit quality. They are included in the compilation of all 90 galaxies in Table 1 and Appendix A, with γ_{outer} in parentheses to indicate that it is measured at $R_{\text{max}} < 20$ kpc rather than at 20 kpc. In the following sections, we will use γ_{outer} only from the 56 galaxies with $R_{\text{max}} > 20$ kpc.

Unusually small radial coverage of the binned data (in kpc) generally stems from some combination of distance (with closer galaxies having a smaller physical FOV) or poor observing conditions (making the signal-to-noise ratio too small in the galaxy outskirts), and so does not cause a bias in stellar mass or environment. About 1/3 of our galaxies are excluded from the analysis of γ_{outer} for having $R_{\text{max}} < 20$ kpc, and we have verified that they reflect the overall sample in distribution of stellar mass and environment.

3.4 Comparison with literature

A number of the MASSIVE galaxies in this paper have published $\sigma(R)$ measurements, typically based on long-slit observations covering a smaller radial extent than our survey. In most cases, our results are reasonably consistent with these earlier measurements over comparable radial ranges, but our more extended data sometimes find different slopes for $\sigma(R)$ in the previously unexplored outer regions. In addition, our IFS data provide kinematic measurements over several angular bins at a given radius. We discuss some specific cases here.

Franx et al. (1989) found falling $\sigma(R)$ profiles for NGC 1700, NGC 4472, and NGC 7619. We also find falling

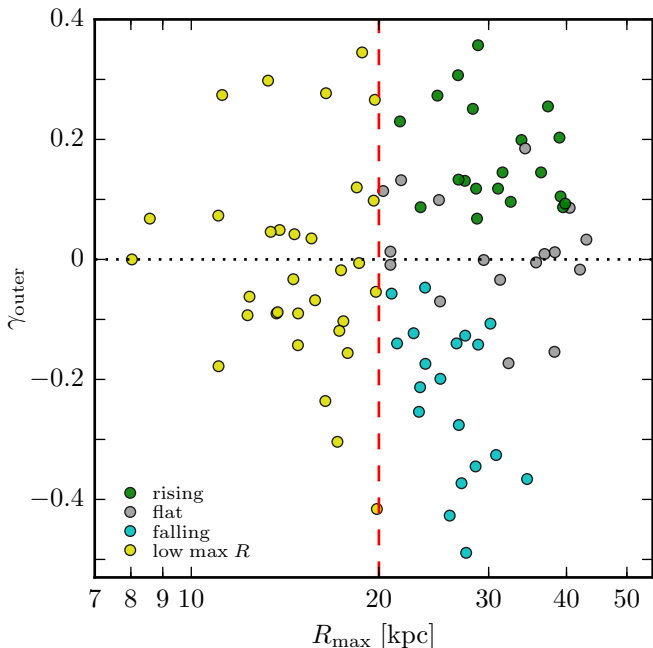


Figure 5. Outer $\sigma(R)$ slope γ_{outer} versus R_{max} , the maximum radius in kpc covered by our IFS data. The fraction of galaxies with rising outer profiles is smaller for galaxies with $R_{\text{max}} < 20$ kpc, and many of those galaxies have uncertain fits (see Appendix A). For those galaxies, γ_{outer} is measured at R_{max} instead of at 20 kpc, so γ_{outer} cannot be fairly compared to the rest of the sample. About 2/3 of our galaxies have $R_{\text{max}} > 20$ kpc, and we restrict our analysis to those galaxies to enable fair comparisons of γ_{outer} across the sample.

$\sigma(R)$ for all three galaxies, though with uniformly steeper power law slopes: $\gamma_{\text{inner}} = -0.09, -0.07, -0.16$, instead of $-0.03, -0.02, -0.08$, respectively. Our galaxies are measured to uniformly larger radii (29, 14, 11 kpc, instead of 10, 2, 9 kpc respectively), and each galaxy behaves differently at these larger radii. NGC 1700 falls more steeply at large radius, while NGC 4472 keeps nearly the same power law slope and NGC 7619 becomes flat.

Fisher et al. (1995) found falling $\sigma(R)$ profiles for NGC 2832, NGC 4073, NGC 4472, NGC 4874, NGC 4889, and NGC 7619, with NGC 4839 nearly flat. Our inner slope γ_{inner} matches reasonably well with their power law slopes in all cases, where our (their) values are -0.09 (-0.07), -0.10 (-0.04), -0.07 (-0.04), -0.03 (-0.09), -0.13 (-0.05), -0.15 (-0.10), and 0.03 (-0.01), respectively. We find a positive outer slope γ_{outer} for all of these except NGC 4472, and in every case our data extends to a larger radius (although not always to 20 kpc). None of their measurements covered beyond 20 kpc except for NGC 2832, which went to ~ 23 kpc. Our data for NGC 2832 extend to 33 kpc and find σ to increase in this outer region.

Another series of papers presented long-slit data of some MASSIVE galaxies (typically to a radius of $\sim 20''$), but did not quote power-law slopes of the σ profiles (Simien & Prugniel 1997, 1998, 2000): NGC 0080, NGC 0410, NGC 0890, NGC 1573, NGC 1684, NGC 2340, NGC 3158, and NGC 5129 were included. Many have large error bars on the σ profiles, but when trends can be discerned, all

galaxies have flat or falling $\sigma(R)$ and agree with our measurements where they overlap. The two possible exceptions are NGC 1684 and NGC 3158. We see a large scatter in σ in the outskirts of NGC 1684, but no coherent increase, so the few outer points from Simien & Prugniel (2000) are likely part of that scatter. For NGC 3158, we do see a small bump in σ at the outskirts of the Simien & Prugniel (1998) measurement, but we find that σ remains flat beyond that radius. Of these 8 galaxies, we find two galaxies (NGC 0080 and NGC 5129) to show rising σ beyond $20''$.

A few individual galaxies have also been studied previously: NGC 1600 (Verolme et al. 2002), NGC 2320 (Cretton et al. 2000), and NGC 2672 (Bonfanti et al. 1995), and they similarly agree with our measurements where they overlap. None of those galaxies show rising σ in our sample. On the other hand, of the five galaxies with data in both this paper and Loubser et al. (2008) (NGC 2832, NGC 3842, NGC 4839, NGC 4874, and NGC 4889), only NGC 3842 does not show a rising outer profile in our data. NGC 4839 shows a rising $\sigma(R)$ but with limited radial bins, and the remaining three all have clear rising outer $\sigma(R)$. In all three cases, our data extend farther than that in Loubser et al. (2008) and agree with their data in the inner regions.

Many galaxies in the Coma cluster have falling $\sigma(R)$ (Thomas et al. 2007), but that paper found all three Coma galaxies in the MASSIVE sample (NGC 4839, NGC 4874, and NGC 4889) to have at least some hint of a rising profile. Of those, NGC 4839 had the most prominent rise, and was also the only galaxy to be measured to (and slightly beyond) R_e . In our sample, the situation is reversed, with NGC 4839 measured to less than 10 kpc while NGC 4874 and NGC 4889 are measured to at least 30 kpc and show a substantial rise in σ .

We have also compared those of our galaxies that overlap with ATLAS^{3D} (NGC 4472, NGC 5322, and NGC 5557) in Appendix B of Veale et al. 2017a and find that all the kinematics (not just σ) match well where they overlap in radius. None of these three galaxies are in the subset of ATLAS^{3D} galaxies studied in the SLUGGS survey (Foster et al. 2016).

4 DISPERSION PROFILES VERSUS VELOCITY KURTOSIS h_4

When interpreting dispersion profiles, the degeneracy between velocity anisotropy and enclosed mass (or mass-to-light ratio) can be somewhat alleviated by examining the kurtosis h_4 of the LOSVD. Radial anisotropy is generally associated with positive h_4 and lower projected σ , while tangential anisotropy is associated with negative h_4 and higher projected σ (Gerhard et al. 1998). Even in isotropic systems, however, positive h_4 can also arise from gradients (of either sign) in circular velocity (Gerhard 1993; Baes et al. 2005). A transition from the galaxy dispersion to cluster dispersion can also be interpreted as a galaxy surrounded by intracluster light (ICL) from a diffuse halo of stars controlled by the cluster gravity, although a clear decomposition into these two components is difficult (Bender et al. 2015). In practice, for cluster BCGs (especially cD galaxies) an ICL component and a circular velocity gradient play similar roles for our purposes, both producing a positive h_4 .

Figure 6 shows that, as we found in Veale et al. (2017a),

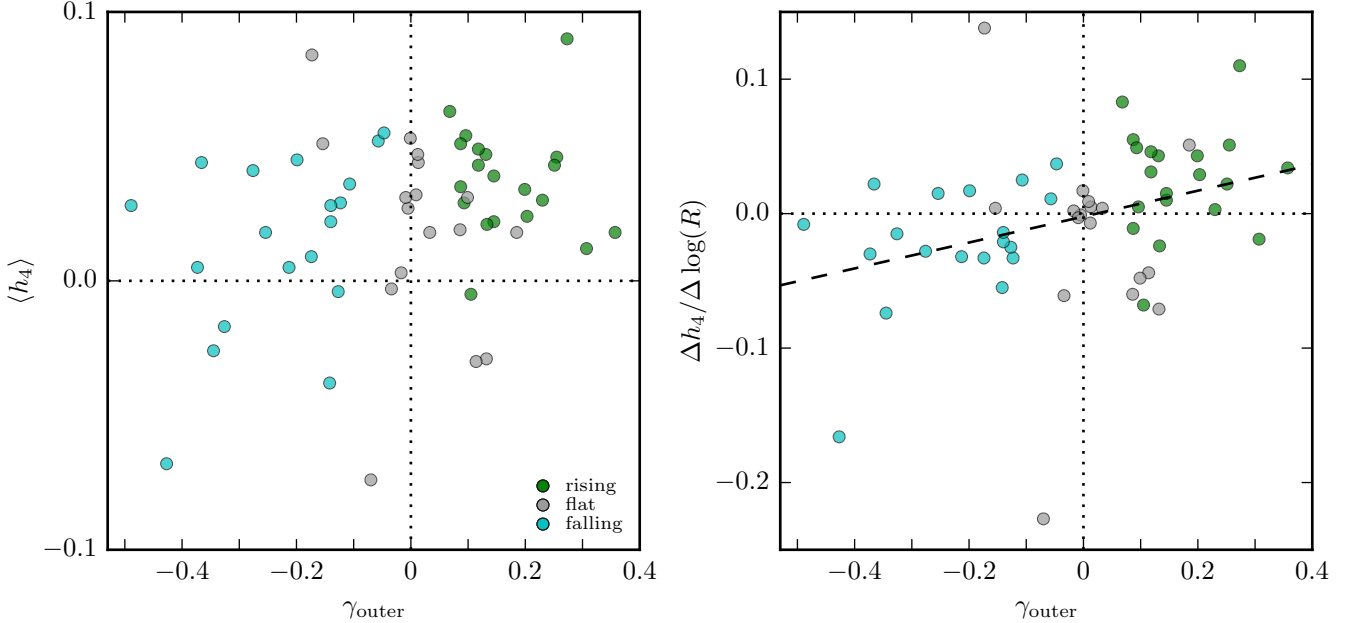


Figure 6. Luminosity-weighted average h_4 within R_e (left) and h_4 gradient (right) versus γ_{outer} . Nearly all galaxies with rising outer $\sigma(R)$ profiles have positive $\langle h_4 \rangle$. There is a positive correlation between h_4 gradient and γ_{outer} (dashed line in right panel) with a slope of 0.096 ± 0.037 , and the corresponding p -value for the significance of the correlation is $p = 0.012$. The few outliers in both panels are perhaps due to limitations on spectral resolution, as they are galaxies with low overall σ .

MASSIVE galaxies have generally positive h_4 and there is evidence for a correlation between outer σ gradient and h_4 gradient. The p -value for the significance of the correlation (with slope 0.096 ± 0.037) is 0.012. One feature not found in Veale et al. (2017a) are the few galaxies with negative $\langle h_4 \rangle$ and substantially negative (< -0.1) gradients in h_4 . These are likely due to low σ , with $\sigma < 200 \text{ km s}^{-1}$ causing large scatter in h_4 because of limitations on wavelength resolution. In particular, the most negative two points in both panels of Figure 6 and the outlying positive h_4 gradient are all galaxies with low average σ . Because Veale et al. (2017a) focused only on the most massive 41 galaxies of the sample, it is not surprising that outliers related to low σ did not arise in that subsample. Formal errors on $\langle h_4 \rangle$ are typically ~ 0.01 , but additional systematic effects are likely present for low σ .

As in Veale et al. (2017a), we argue the correlation between the h_4 gradient and γ_{outer} is much more likely to be a consequence of circular velocity gradients (or an ICL component) than velocity anisotropy. If all galaxies had similar mass (and light) profiles, then a positive h_4 gradient related to greater radial anisotropy at large radius would be expected to accompany a more *negative* σ gradient, and so cannot explain the observed correlation. It is also true that tangential anisotropy can only boost σ by a limited amount, and in particular cannot boost it above the circular velocity. This makes invoking radial anisotropy to explain low σ more easily justified in most cases than invoking tangential anisotropy to explain high σ . For these reasons, we argue that variations in the total mass profiles across our sample (and variations from isothermal profiles) are likely present.

In this context, our positive $\langle h_4 \rangle$ could result from ei-

ther mass profiles (V_{circ} gradients, ICL components) or radial anisotropy, or some combination of both. If mass profiles are the dominant effect on h_4 , then in principle *tangential* anisotropy may also be common in our sample in spite of the overall positive h_4 . Based on our data, we can make no claims about the anisotropy of our sample as a whole, or about changes in anisotropy across our sample, without more detailed dynamical modeling. We leave such modeling for future papers.

5 DISPERSION PROFILES VERSUS GALAXY MASS AND ENVIRONMENT

5.1 σ profiles and stellar mass M_*

Figure 7 shows the power law slope of $\sigma(R)$ at 2 kpc (γ_{inner} , left) and 20 kpc (γ_{outer} , right) versus stellar mass M_* (and M_K) for the 90 MASSIVE galaxies (56 of which have data reaching to 20 kpc; see Section 3.3). Most galaxies have falling $\sigma(R)$ in the inner part ($\gamma_{\text{inner}} \lesssim 0$), but the outer $\sigma(R)$ has slopes spanning $-0.4 \lesssim \gamma_{\text{outer}} \lesssim 0.3$. Thick black pentagons indicate the average values of γ_{inner} and γ_{outer} for each of three M_* bins. Both γ_{inner} and γ_{outer} show a positive trend with M_* , but the trend with γ_{outer} is much steeper. In particular, only one of the 11 most massive galaxies has a falling profile, and it is very shallow. A direct linear fit gives a slope of $0.056 \pm 0.030 \text{ mag}^{-1}$ for γ_{inner} versus M_K , and $0.170 \pm 0.083 \text{ mag}^{-1}$ for γ_{outer} versus M_K . A simple linear model is clearly inappropriate for the relationship with γ_{outer} versus M_K , where the overall scatter relative to the fit is ~ 0.19 (much larger than the typical errors on γ_{outer}) and

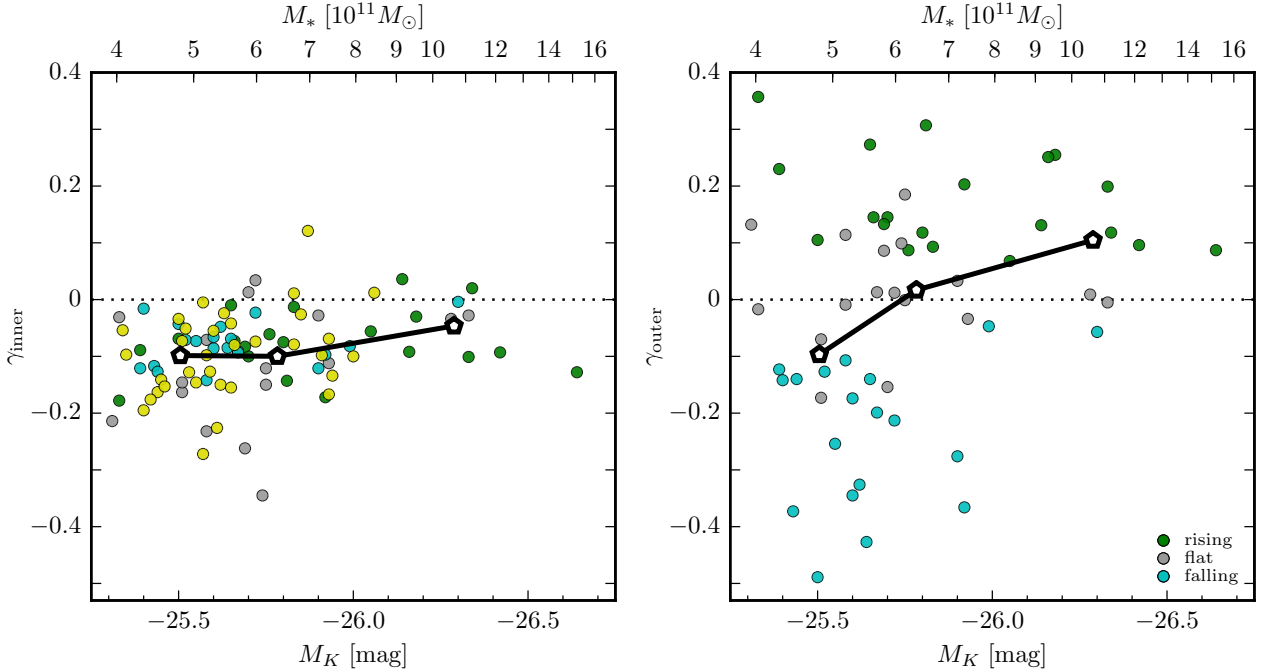


Figure 7. Inner (left) and outer (right) slopes of $\sigma(R)$ versus M_* (and M_K). The inner σ profiles are mostly falling, in the range of $-0.2 < \gamma_{\text{inner}} < 0$, with an average power-law slope (thick black pentagons) of -0.1 becoming more shallow at -0.05 in the highest M_* bin. Galaxies with $R_{\text{max}} < 20$ kpc (yellow; left out of γ_{outer} sample) have a similar distribution of γ_{inner} as the other galaxies. The outer slopes γ_{outer} span a larger range of about -0.4 to $+0.3$ at the low end of the mass range, but are mostly positive at $M_* \gtrsim 8 \times 10^{11} M_\odot$. Rising outer profiles are found across the whole mass range, whereas falling outer profiles are found only for galaxies with $M_* \lesssim 8 \times 10^{11} M_\odot$, leading to a correlation between average γ_{outer} and M_* .

varies substantially with M_K . To investigate the relationship another way, Figure 8 shows the fraction of galaxies with rising (green), flat (grey), and falling (cyan) outer $\sigma(R)$ for the three M_* bins. The error bars³ in Figure 8 reflect the uncertainty due to small number statistics in each bin.

As discussed in Section 4, detailed mass modeling would be needed to determine whether the correlations between γ_{outer} and M_* seen in Figure 7 and Figure 8 indicate mass profile changes, or velocity anisotropy variations, or both. Dynamical and lensing measurements have found roughly isothermal total mass profiles for many elliptical galaxies, especially within one or two R_e (Gerhard et al. 2001; Treu et al. 2006; Koopmans et al. 2009; Auger et al. 2009, 2010; Thomas et al. 2011; Sonnenfeld et al. 2013; Cappellari et al. 2015). But there is some evidence that smaller galaxies may have steeper than isothermal mass profiles (Romanowsky et al. 2003; Napolitano et al. 2009; Deason et al. 2012; Morganti et al. 2013; Alabi et al. 2016), whereas more massive galaxies may have shallower than isothermal profiles (Newman et al. 2013). Simulations have suggested that merger histories may influence velocity anisotropy (Dekel et al. 2005; Wu et al. 2014), so the fact that more massive galaxies have a more extensive merger history may also link mass to velocity anisotropy.

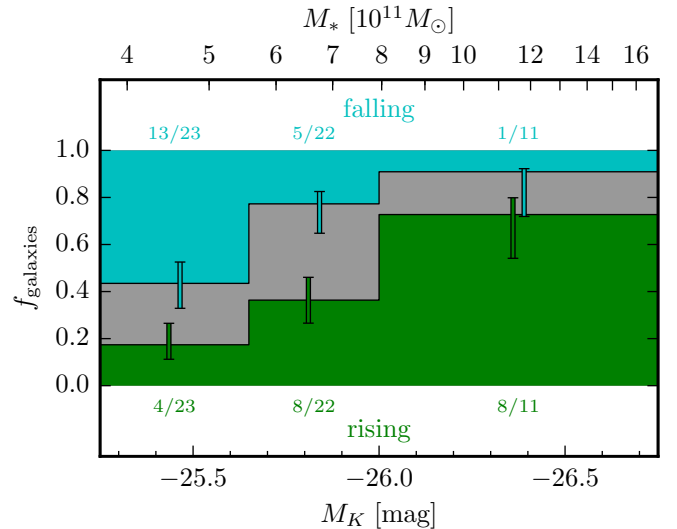


Figure 8. Fraction of rising (green), flat (grey), and falling (cyan) outer σ profiles versus M_K and M_* . In spite of the narrow mass range of our sample, there is a strong correlation between outer $\sigma(R)$ profile behaviour and stellar mass.

³ Error bars are calculated as described in Appendix B of Veale et al. (2017b), with a Beta distribution as prior and posterior. We use $n_{\text{prior}} = 2$ for a very weak prior, and μ_{prior} is the total sample fraction of rising (20/56) or falling (19/56) profiles.

In all of these cases, it is important to keep in mind the physical scale under consideration: at small radii, central supermassive black holes become important, while stars dominate at intermediate radii and dark matter dominates

Table 2. Two-sample Kolmogorov-Smirnov test D statistic and p values for comparing the distribution in M_* or environment of the galaxy sample, split into two samples of galaxies by separating first rising profiles (left columns) and then falling profiles (right columns).

	(rising v. flat+falling)		(rising+flat v. falling)	
	D -statistic	p -value	D -statistic	p -value
M_K	0.428	0.012	0.414	0.019
M_{halo}	0.385	0.032	0.338	0.088
δ_g	0.361	0.052	0.263	0.301
ν_{10}	0.467	0.005	0.289	0.205

at large radii. For example, core scouring by merging super-massive black holes likely impacts the σ profiles near the galaxy center (Thomas et al. 2014) and may relate to γ_{inner} . The IFS data presented here do not resolve the galaxy cores, however, so we will not consider further the central regions of the galaxy and γ_{inner} . In the following sections we focus instead on how the outer σ profiles (i.e. γ_{outer}) may correlate with galaxy environment and dark matter.

5.2 Outer σ profiles vs. environmental measures

M_{halo} , δ_g , and ν_{10}

Figure 9 shows the power law σ slope at 20 kpc (γ_{outer} , upper panels) and the fraction of galaxies with rising, flat, and falling outer σ profiles (lower panels) versus three environmental variables: halo mass M_{halo} (left), large-scale overdensity δ_g (middle), and local density ν_{10} (right). Within each upper panel, the average γ_{outer} for three environmental bins is shown as thick black pentagons. All panels show clear trends of increasing f_{rising} , increasing average γ_{outer} , and decreasing f_{falling} in denser environments, and the trend is most prominent for M_{halo} . Simple linear fits of γ_{outer} versus each environment variable give distinctly positive slopes (0.126 ± 0.036 , 0.193 ± 0.093 , and $0.043 \pm 0.017 \text{ dex}^{-1}$ for M_{halo} , δ_g , and ν_{10} respectively), similar to the case with M_K in the previous section, and again the scatter around each linear fit is much larger than the typical errors on γ_{outer} .

The upper panels of Figure 9 also show that galaxies with steeply rising outer $\sigma(R)$ are found preferentially in high density environments, while galaxies with steeply declining outer $\sigma(R)$ span a wide range of environments. In terms of halo mass, the galaxies with rising γ_{outer} have an average M_{halo} of $4.7 \times 10^{14} M_{\odot}$, about four times more massive than the average M_{halo} of $1.2 \times 10^{14} M_{\odot}$ for galaxies with falling γ_{outer} .

We have performed a two-sample Kolmogorov-Smirnov (KS) test to compare the distributions of galaxy mass and environments, first comparing galaxies with rising profiles to those with flat or falling profiles, and second comparing galaxies with falling profiles to those with flat or rising ones. Table 2 shows both the D statistic, which measures the maximum difference between the empirical cumulative distribution functions of the two samples, and the p -value, which quantifies the significance of that difference taking into account sample size.⁴

⁴ We have adjusted the p -value of the KS test for distributions

We find that the most significant difference between the samples is related to the increase in f_{rising} with increasing ν_{10} , with $p \sim 0.005$. The next two most significant differences are related to stellar mass, with f_{rising} increasing ($p \sim 0.012$) and f_{falling} decreasing ($p \sim 0.019$) at higher mass/brighter M_K . There is an interesting feature of separating strongly rising and falling profiles from flat ones: while M_* has comparable p -values whether separating rising profiles or falling ones, the environment measures tend to have much worse p -values for separating falling profiles. This indicates that different mechanisms may be behind the trends, and we will discuss this further in Section 6.

Much like the situation with M_* in Section 5.1, the correlation between σ profile behaviour and environment may be related to changing mass and luminosity profiles, changing velocity anisotropy, or both. Based on our results in Section 4, we find it unlikely that anisotropy alone can be behind the correlation. Instead, we interpret this as evidence that galaxies in more massive haloes may have total mass profiles that are shallower than isothermal, while those in less massive haloes have the more “typical” isothermal profiles. Some lensing results have also suggested this (Newman et al. 2015). We cannot entirely rule out anisotropy playing some role, however. The connection between merging history and anisotropy may also result in a connection between environment and anisotropy, since galaxies in more dense environments likely experience a more extensive merger history. This parallels our discussion from Section 5.1, and indeed the correlation between M_* and environment makes the two arguments equivalent to some degree. We will explore in the next sections how to distinguish whether trends with environment are simply a reflection of trends in M_* , or vice versa, or whether both are independent.

5.3 Outer σ profiles vs. group membership

Figure 10 and Figure 11 show $\sigma(R)$ for the 90 MASSIVE galaxies sorted by group membership, i.e., whether it is the brightest galaxy or a satellite in a group/cluster, or it is relatively isolated. The differences in the fractions of rising or falling profiles for the three types are small in comparison to the differences with M_* or M_{halo} .

The right side of Figure 11 shows the γ_{outer} versus M_* and M_{halo} panels of Figure 7 and Figure 9, but with group membership marked with additional symbols (magenta squares are isolated; orange diamonds are satellites; unmarked galaxies are all BGGs). The satellite galaxies in our sample, as expected, are found only in the higher mass haloes ($M_{\text{halo}} \gtrsim 10^{14} M_{\odot}$); in the lower mass haloes, only the BGGs are luminous enough to pass our survey magnitude cutoff. Satellite galaxies also reside in the lower part of the M_* range. The average γ_{outer} for satellite galaxies is slightly higher than that for BGGs or isolated galaxies, reflecting the typical γ_{outer} of galaxies in massive haloes more than the

in M_{halo} to account for the reduced sample size, due to some galaxies being isolated with no measurement of M_{halo} available, by using the full sample size including isolated galaxies when converting the D -statistic to a p -value. This reduces the p -values from $\sim 0.06, 0.17$ to $\sim 0.03, 0.09$.

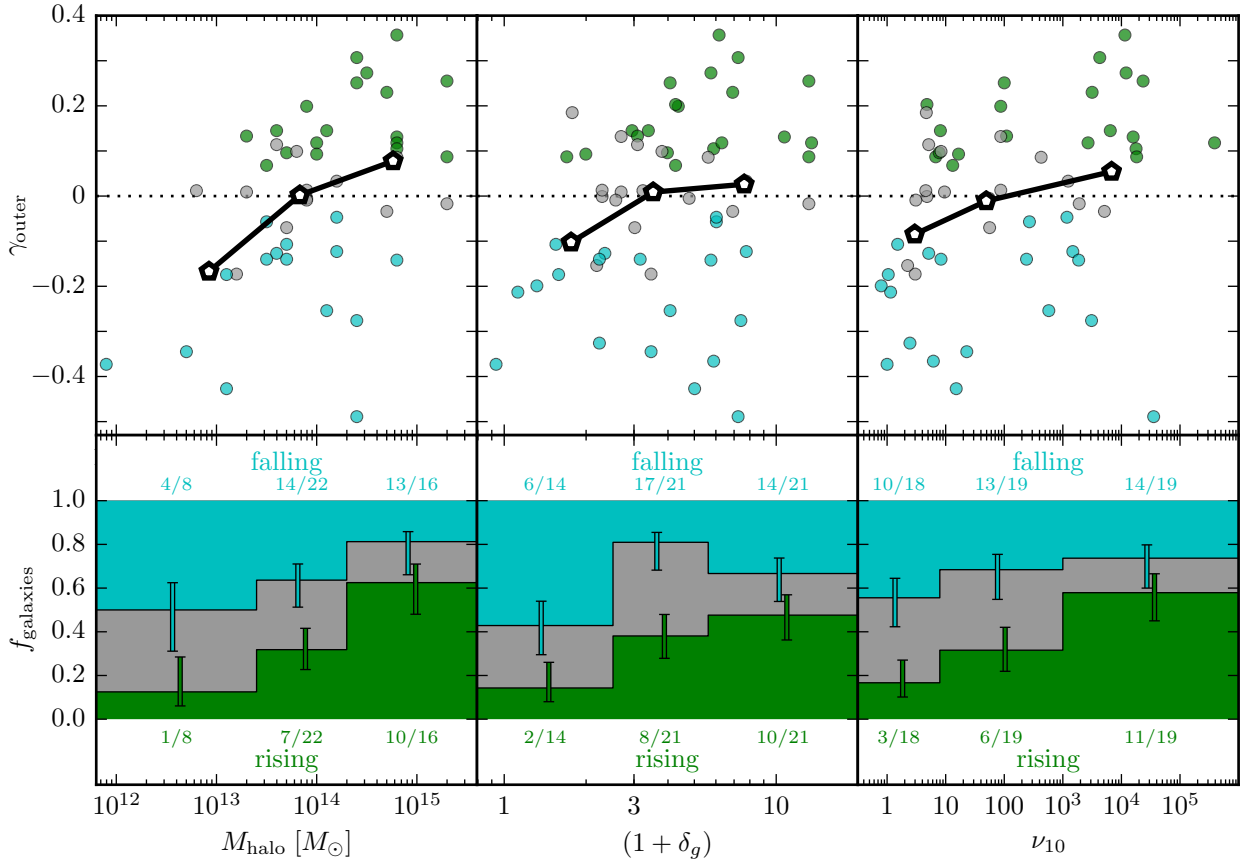


Figure 9. Outer $\sigma(R)$ profile behavior versus three environment measures: M_{halo} (left), large-scale density δ_g (middle), and local density ν_{10} (right). The top panels show γ_{outer} ; the bottom panels show the fraction of rising (green), flat (grey), and falling (cyan) outer profiles. For all three environmental measures, f_{rising} and average γ_{outer} (open black pentagons) increase in more dense environments, and f_{falling} decreases correspondingly. The most steeply rising outer profiles are also found in the highest density environments, while steeply falling profiles are found in a wide range of environments.

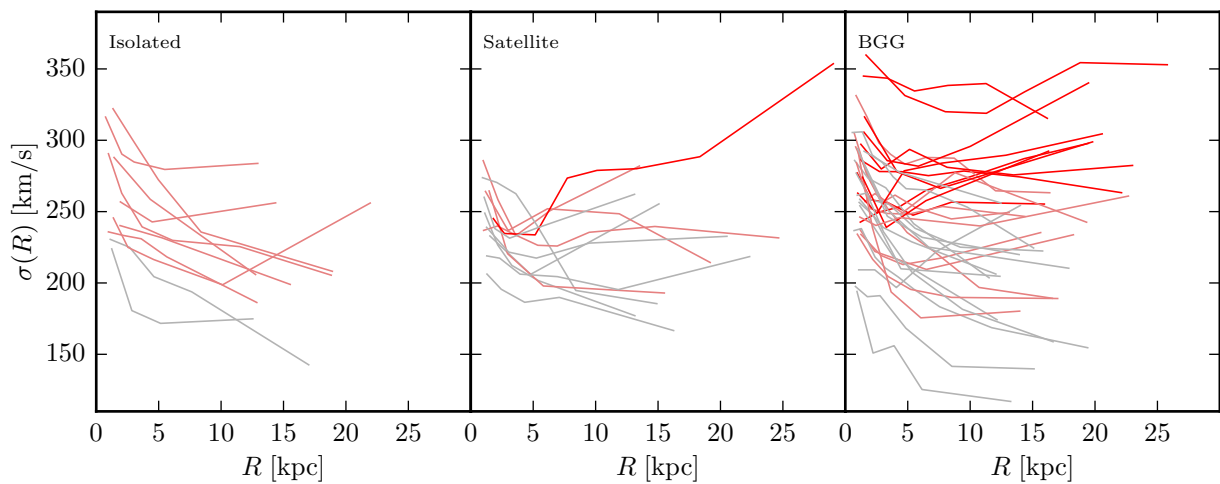


Figure 10. Dispersion profiles as in Figure 1, but separated by group membership status. The line colors correspond to the 3 bins of M_* in Figure 8, with grey for the least massive and red for the most massive. The outermost point represents the average radius of the outermost bin; the total radial extent of the data is up to $\sim 60\%$ larger. Ten of the most massive 11 galaxies in our sample are BGGs; the exception is NGC 4874, the second brightest galaxy in the Coma cluster.

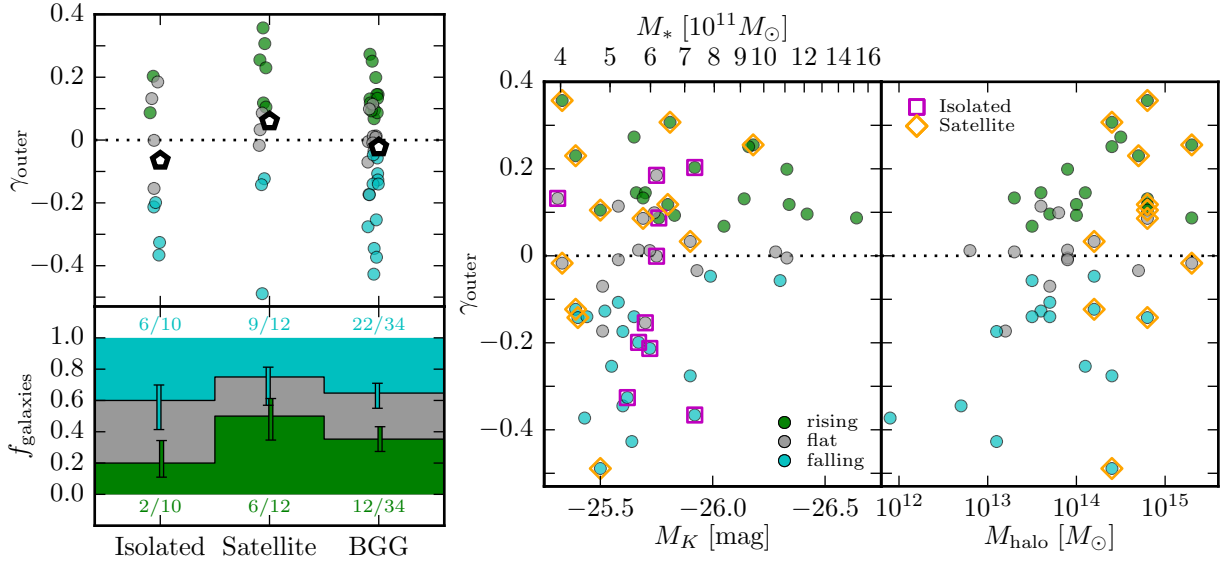


Figure 11. Outer slope γ_{outer} and fraction of rising (green), flat (grey), and falling (cyan) galaxies versus group membership status (left panels), and γ_{outer} versus stellar and halo masses with group membership highlighted (right panels). The average γ_{outer} (open black pentagons) is slightly higher for satellite galaxies (yellow diamonds in right panel), which include the most steeply rising σ profiles.

typical behaviour of low mass galaxies. Many of the most steeply rising profiles are found in satellite galaxies.

The physical significance of rising σ in BGG and satellite galaxies may be different, especially if rising σ is connected to the total mass profiles. In many discussions (e.g. Bender et al. 2015) the focus is on a central galaxy in a large cluster, and the total mass profile is simply the combination of stellar mass and the dark matter of the cluster halo. Ongoing detailed mass modeling of our satellite galaxies will help elucidate the impact of the group or cluster halo mass on a non-central galaxy, which may have its own dark matter subhalo or be moving at a substantial velocity relative to the group or cluster rest frame. Some of our BGGs may also not be central galaxies (e.g. Skibba et al. 2011; Hoshino et al. 2015), and cases where the two brightest galaxies are nearly matched in luminosity are also of interest.

Figure 11 shows that 2 of the 10 isolated galaxies in our sample with γ_{outer} measured at 20 kpc have distinctly rising profiles: NGC 2693 and NGC 5129. NGC 2693 is only marginally inconsistent with $\gamma_{\text{outer}} = 0$, with $\gamma_{\text{outer}} = 0.087 \pm 0.065$, while NGC 5129 has $\gamma_{\text{outer}} = 0.203 \pm 0.085$. Both galaxies are at fairly large distances (74 and 108 Mpc, respectively). If we assume they are BGGs of groups whose rank 3 members fall just below the 2MASS limit, they will have luminosity gaps (~ 2.0 mag and 2.7 mag respectively) comparable to those found for some other BGGs in our sample. Only about 10 of our 85 galaxies have luminosity gaps (between rank 1 and rank 3) as large as 2.0 mag, and only 5 of those gaps as large as 2.5 mag. All 10 of those galaxies have $M_{\text{halo}} < 10^{14} M_\odot$. These two isolated galaxies would thus be unusually fossil-like if they reside in halos of $M_{\text{halo}} \gtrsim 10^{14} M_\odot$. If they instead reside in smaller halos, their group composition may be comparable to that of many BGGs in our sample, but they would then have γ_{outer} as high or higher than all our other BGGs at those halo masses.

5.4 Untangling the joint relationships of M_* and M_{halo}

In this section we consider two opposing, extreme assumptions: first, that the probability of a galaxy having a rising σ profile (denoted P_{rising}) is a function of M_* (or M_K) only, and second, that it is a function of ν_{10} only. If $P_{\text{rising}} = P_{\text{rising}}(M_*)$, and ν_{10} plays no direct/independent role in influencing the σ profile, we still expect some residual correlation between the measured fraction of rising profiles (f_{rising}) and ν_{10} . This arises because the distribution of M_* changes with ν_{10} for our sample, so convolving $P_{\text{rising}}(M_*)$ with that distribution gives a fraction of rising profiles that depends on ν_{10} . The reverse also applies: if $P_{\text{rising}} = P_{\text{rising}}(\nu_{10})$ then the connection between ν_{10} and M_* results in some correlation between f_{rising} and M_* .

Figure 12 compares the “predictions” of each of these extreme assumptions with the actual measured f_{rising} . The test samples used to calculate f_{rising} for the two assumptions (i.e. using $P_{\text{rising}}(M_*)$ and $P_{\text{rising}}(\nu_{10})$) are constructed by assigning each galaxy in our sample a *probability* of having a rising profile, then running 1000 Monte Carlo trials assigning falling/rising profiles according to those probabilities and counting the resulting fractions in each bin. $P_{\text{rising}}(M_*)$ is constructed by fitting a logistic function to the unbinned M_* data (where falling profiles are 0 and rising profiles are 1), and similarly for ν_{10} .

In each case, the test sample accounts for only a tiny amount of the increase in f_{rising} with M_* or ν_{10} , indicating that both stellar mass and environment are responsible for the trends in f_{rising} . The relatively small number statistics in each bin result in substantial estimates of the error, so the actual f_{rising} and test sample f_{rising} in each individual bin have errors overlapping at least slightly. However, the overall behaviour of f_{rising} versus M_* and ν_{10} is very different between the nearly flat test samples and the correlations in the actual data. This is in contrast to the case of fast and slow

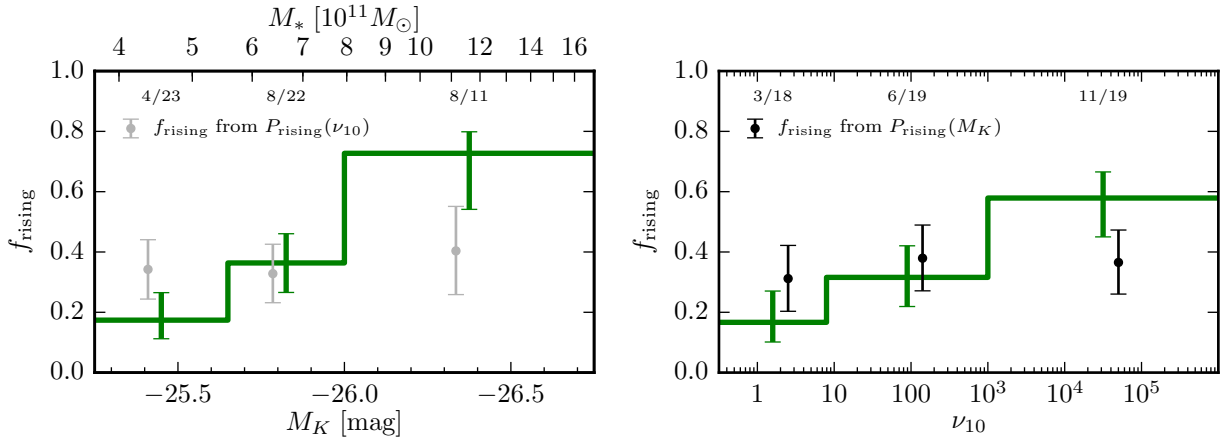


Figure 12. Comparing the assumptions that the probability of having a rising $\sigma(R)$ profile (P_{rising}) is a function of ν_{10} only (gray; left panel), or a function of M_K only (black; right panel). In each case P_{rising} is a logistic function fit to the data, with each galaxy at 0 (falling) or 1 (rising), so it is independent of the choice of binning. P_{rising} is used to calculate f_{rising} via 1000 Monte Carlo trials (see text). This is compared to the actual measured f_{rising} (green lines), with points offset slightly in the x-direction for clarity. The assumption that P_{rising} is a function only of ν_{10} does not predict the observed sharp increase in f_{rising} with M_K (left panel). Likewise, the assumption that P_{rising} is a function only of M_K produces only a tiny increase in f_{rising} versus M_{halo} , not enough to match the data (right panel). Both stellar mass and environment therefore drive the observed trend in f_{rising} .

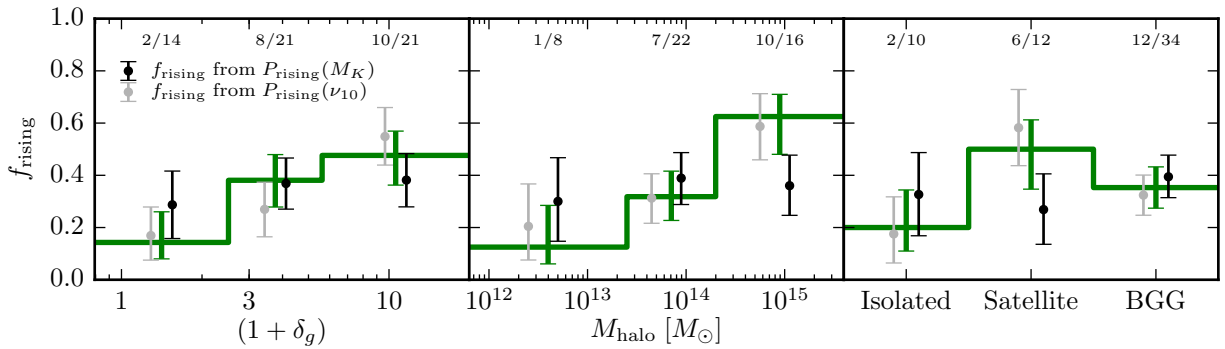


Figure 13. Comparing how well f_{rising} versus δ_g , M_{halo} and group membership status is reproduced under the assumption that P_{rising} is a function of M_K only (black) or of ν_{10} only (gray). The gray points can reproduce the actual measured f_{rising} in every case, as might be expected due to the correlations among different measures of environment. Points within each bin are offset slightly for clarity.

rotators in [Veale et al. \(2017b\)](#), where M_* alone determines P_{slow} (within errors). It also differs from the case of f_{falling} in this paper; unsurprisingly, since the change in f_{falling} is much steeper for M_K than ν_{10} , we find that using $P_{\text{falling}}(M_*)$ to construct $f_{\text{falling}}(\nu_{10})$ is consistent with the observed fraction, while using $P_{\text{falling}}(\nu_{10})$ to construct $f_{\text{falling}}(M_*)$ does not account for the observed fraction.

We can also ask whether $P_{\text{rising}}(M_*)$ or $P_{\text{rising}}(\nu_{10})$ does better at “predicting” the fraction of galaxies with rising profiles as a function of the other environment measures. [Figure 13](#) shows that $P_{\text{rising}}(\nu_{10})$ generates f_{rising} versus δ_g , M_{halo} , and group membership that matches better to the data. This is not surprising because ν_{10} is very well correlated with M_{halo} and thus with group membership status, and also correlates with δ_g very closely at low density.

6 CONCLUSIONS

We have measured and characterized the line-of-sight stellar velocity dispersion profiles $\sigma(R)$ of 90 early-type galaxies in the MASSIVE survey, spanning K -band magnitude $-25.3 > M_K > -26.7$, or stellar mass $4 \times 10^{11} M_{\odot} < M_* < 2 \times 10^{12} M_{\odot}$. Our IFS data cover $107'' \times 107''$ field of view and extend up to 40 kpc in radii, with most galaxies in the 15–30 kpc range. We find a radial coverage to ~ 20 kpc or beyond is necessary to measure the outer dispersion profiles of local massive ETGs in a consistent way across the sample ([Figure 5](#)).

We find a variety of shapes for $\sigma(R)$: monotonically falling and rising profiles, U-shaped profiles that fall to a minimum before flattening or rising at large radius, and profiles that are nearly flat in the center and fall at large radius. We quantify the shapes of $\sigma(R)$ with an inner logarithmic slope at 2 kpc (γ_{inner}) and an outer logarithmic slope at 20 kpc (γ_{outer}). Of the 90 galaxies in our sample, 56 have binned data reaching at least 20 kpc, and we limit our analysis of γ_{outer} to those galaxies. All but 1 galaxy in

our sample have γ_{inner} that is negative or consistent with zero (Figure 3 and Table 1), and most are in the range $-0.2 < \gamma_{\text{inner}} < 0$. By contrast, γ_{outer} ranges from ~ -0.5 to $+0.4$, where 36% have rising outer $\sigma(R)$ ($\gamma_{\text{outer}} > 0$), 30% have flat profiles ($\gamma_{\text{outer}} = 0$ within errors), and 34% have falling profiles ($\gamma_{\text{outer}} < 0$; Figure 3).

We show that the fraction of galaxies with rising outer $\sigma(R)$ profiles increases significantly over our M_* range (Figure 7, Figure 8). That fraction also increases in denser environments, as quantified by halo mass M_{halo} , large-scale density δ_g , and local density ν_{10} (Figure 9). Among those, the trend is most prominent with M_{halo} and ν_{10} , with the steepest rising profiles belonging to galaxies in the most dense environments.

We find that the probability of a galaxy having a rising outer σ profile cannot be adequately expressed as either a function of M_* alone or as a function of ν_{10} alone (Figure 12). Both M_* and environment are therefore responsible for driving the trends in the rising fraction. This is to be contrasted with galaxy rotation in the previous MASSIVE paper (Veale et al. 2017b), where the sharp increase in the fraction of slow rotators with M_* is enough to explain the correlation between galaxy rotation and all environmental measures. The first and second velocity moments of massive galaxies therefore reflect different aspects of their past assembly histories.

We find a higher fraction of galaxies with $\gamma_{\text{outer}} > 0$ among satellite galaxies than among BGGs, and a lower fraction among isolated galaxies (Figure 11). Rising dispersion profiles are not limited to BGGs but are found for all three types, although the two isolated galaxies with rising profiles may be the BGGs of groups only slightly more “fossil-like” than others in our sample (Section 5.3). Compared to the BGGs, the satellite galaxies in our sample occupy the lower part of the M_* range (middle panel of Figure 11) but the upper part of the M_{halo} range (right panel of Figure 11). Since the fraction of rising dispersion profiles increases with both M_* and M_{halo} for the galaxies in our study as a whole, these two factors have a competing influence on the fraction of satellites with rising profiles. The satellite galaxies appear to follow the typical behaviour of galaxies at high M_{halo} rather than low M_* , but our sample size is not large enough to say definitively whether satellite galaxies truly have fewer $\sigma(R)$ profiles with $\gamma_{\text{outer}} < 0$ at fixed mass than the overall sample. Future larger surveys can provide important new insights by comparing the kinematics of BGGs, satellites, and isolated galaxies at fixed M_* and M_{halo} .

We find a positive correlation between the outer σ gradient γ_{outer} and the gradient of the LOSVD kurtosis $\Delta h_4 / \Delta \log R$ (Figure 6). Based in part on this correlation, we argue that the rising σ profiles seen in our galaxies and the trends with M_* and environment are likely caused at least in part by variations in total mass profiles (including variations from isothermal). It is unlikely that rising σ profiles can be explained by tangential velocity anisotropy alone, but a positive gradient in circular velocity is consistent with both positive σ gradients and positive h_4 gradients. Our results can accommodate a range of velocity anisotropy, so long as any tangential anisotropy (associated with negative h_4) is not extreme enough to overcome gradients in circular velocity (associated with positive h_4) as the primary influence on $\langle h_4 \rangle$, which we find to be generally positive.

Most likely, both mass profile shape and velocity anisotropy play a role in determining the σ profile. More detailed modeling is required to make any definitive statements, but the correlations with galaxy mass and environment suggest at least one possible scenario. Figure 9 shows an apparently sharp cutoff of the maximum allowed γ_{outer} that increases with M_{halo} , and to a lesser extent with δ_g and ν_{10} . Perhaps this is because the galaxy environment controls the underlying total mass profile shape (in central galaxies) and the presence of non-equilibrium motions (in satellites moving with respect to the cluster), with the surrounding dark matter dictating the maximum possible rise of outer $\sigma(R)$. Figure 7 shows a similar cutoff for the *minimum* allowed γ_{outer} , which increases with M_K . Perhaps this is because substantial radial anisotropy, likely needed to explain very steeply falling σ , cannot survive the extensive merger histories typical of very massive galaxies. At the most extreme masses nearly every galaxy may converge on a homologous anisotropy profile - not necessarily isotropic, but with less extreme radial anisotropy at large radii - while lower mass galaxies show a range of anisotropy profiles. This scenario is consistent with the fact that our observed h_4 implies some variation in mass profiles and can accommodate a range of anisotropy. It is also consistent with how the classification of “flat” profiles impacts the correlations, with f_{rising} correlating more strongly than f_{falling} with M_{halo} , while f_{falling} correlates more strongly than f_{rising} with M_* .

This scenario is again speculative, based on qualitative arguments about the connections among enclosed mass, σ , velocity anisotropy, and h_4 that have been noted in the literature. Our ongoing dynamical modeling efforts using the reported kinematics will provide deeper insights into the trends reported in this paper.

ACKNOWLEDGEMENTS

We thank Marijn Franx for useful discussions, and the anonymous referee for helpful comments. The MASSIVE survey is supported in part by NSF AST-1411945, NSF AST-1411642, HST-GO-14210, and HST-AR-1457.

REFERENCES

- Alabi A. B., et al., 2016, *MNRAS*, **460**, 3838
- Arnold J. A., et al., 2014, *ApJ*, **791**, 80
- Auger M. W., Treu T., Bolton A. S., Gavazzi R., Koopmans L. V. E., Marshall P. J., Bundy K., Moustakas L. A., 2009, *ApJ*, **705**, 1099
- Auger M. W., Treu T., Bolton A. S., Gavazzi R., Koopmans L. V. E., Marshall P. J., Moustakas L. A., Burles S., 2010, *ApJ*, **724**, 511
- Baes M., Dejonghe H., Buyle P., 2005, *A&A*, **432**, 411
- Bender R., Kormendy J., Cornell M. E., Fisher D. B., 2015, *ApJ*, **807**, 56
- Binney J., Mamon G. A., 1982, *MNRAS*, **200**, 361
- Bonfanti P., Rampazzo R., Combes F., Prugniel P., Sulentic J. W., 1995, *A&A*, **297**, 28
- Brodie J. P., et al., 2014, *ApJ*, **796**, 52
- Brough S., Proctor R., Forbes D. A., Couch W. J., Collins C. A., Burke D. J., Mann R. G., 2007, *MNRAS*, **378**, 1507
- Burke C., Collins C. A., 2013, *MNRAS*, **434**, 2856
- Cappellari M., 2013, *ApJ*, **778**, L2

- Cappellari M., Emsellem E., 2004, *PASP*, **116**, 138
- Cappellari M., et al., 2015, *ApJ*, **804**, L21
- Carrick J., Turnbull S. J., Lavaux G., Hudson M. J., 2015, *MNRAS*, **450**, 317
- Carter D., Efstathiou G., Ellis R. S., Inglis I., Godwin J., 1981, *MNRAS*, **195**, 15P
- Carter D., Inglis I., Ellis R. S., Efstathiou G., Godwin J. G., 1985, *MNRAS*, **212**, 471
- Carter D., Bridges T. J., Hau G. K. T., 1999, *MNRAS*, **307**, 131
- Cohen J. G., Ryzhov A., 1997, *ApJ*, **486**, 230
- Côté P., et al., 2001, *ApJ*, **559**, 828
- Côté P., McLaughlin D. E., Cohen J. G., Blakeslee J. P., 2003, *ApJ*, **591**, 850
- Cretton N., Rix H.-W., de Zeeuw P. T., 2000, *ApJ*, **536**, 319
- Crook A. C., Huchra J. P., Martimbeau N., Masters K. L., Jarrett T., Macri L. M., 2007, *ApJ*, **655**, 790
- Crook A. C., Huchra J. P., Martimbeau N., Masters K. L., Jarrett T., Macri L. M., 2008, *ApJ*, **685**, 1320
- Davies R. L., Illingworth G., 1983, *ApJ*, **266**, 516
- Davies R. L., Illingworth G. D., 1986, *ApJ*, **302**, 234
- Davis T. A., Greene J., Ma C.-P., Pandya V., Blakeslee J. P., McConnell N., Thomas J., 2016, *MNRAS*, **455**, 214
- Deason A. J., Belokurov V., Evans N. W., McCarthy I. G., 2012, *ApJ*, **748**, 2
- Dejonghe H., Merritt D., 1992, *ApJ*, **391**, 531
- Dekel A., Stoehr F., Mamon G. A., Cox T. J., Novak G. S., Primack J. R., 2005, *Nature*, **437**, 707
- Dressler A., 1979, *ApJ*, **231**, 659
- Durrell P. R., et al., 2014, *ApJ*, **794**, 103
- Edwards L. O. V., Patton D. R., 2012, *MNRAS*, **425**, 287
- Emsellem E., et al., 2011, *MNRAS*, **414**, 888
- Faber S. M., Burstein D., Dressler A., 1977, *AJ*, **82**, 941
- Falco M., Hansen S. H., Wojtak R., Brinckmann T., Lindholmer M., Pandolfi S., 2014, *MNRAS*, **442**, 1887
- Ferrarese L., et al., 2012, *ApJS*, **200**, 4
- Fisher D., Illingworth G., Franx M., 1995, *ApJ*, **438**, 539
- Foster C., et al., 2016, *MNRAS*, **457**, 147
- Franx M., Illingworth G., Heckman T., 1989, *ApJ*, **344**, 613
- Gerhard O. E., 1993, *MNRAS*, **265**, 213
- Gerhard O., Jeske G., Saglia R. P., Bender R., 1998, *MNRAS*, **295**, 197
- Gerhard O., Kronawitter A., Saglia R. P., Bender R., 2001, *AJ*, **121**, 1936
- Goulding A. D., et al., 2016, *ApJ*, **826**, 167
- Greene J. E., Janish R., Ma C.-P., McConnell N. J., Blakeslee J. P., Thomas J., Murphy J. D., 2015, *ApJ*, **807**, 11
- Hau G. K. T., Hilker M., Bridges T., Carter D., Dejonghe H., de Rijcke S., Quintana H., 2004, in Diaferio A., ed., *IAU Colloq. 195: Outskirts of Galaxy Clusters: Intense Life in the Suburbs*. pp 491–495, doi:10.1017/S1743921304001061
- Heisler J., Tremaine S., Bahcall J. N., 1985, *ApJ*, **298**, 8
- Hill G. J., et al., 2008, in *Society of Photo-Optical Instrumentation Engineers (SPIE) Conference Series*. , doi:10.1117/12.790235
- Hoshino H., et al., 2015, *MNRAS*, **452**, 998
- Huchra J., et al., 2005a, in Colless M., Staveley-Smith L., Stathakis R. A., eds, *IAU Symposium Vol. 216, Maps of the Cosmos*. p. 170
- Huchra J., et al., 2005b, in Fairall A. P., Woudt P. A., eds, *Astronomical Society of the Pacific Conference Series Vol. 329, Nearby Large-Scale Structures and the Zone of Avoidance*. p. Fairall
- Huchra J. P., et al., 2012, *ApJS*, **199**, 26
- Jarrett T. H., Chester T., Cutri R., Schneider S., Skrutskie M., Huchra J. P., 2000, *AJ*, **119**, 2498
- Kelson D. D., Zabludoff A. I., Williams K. A., Trager S. C., Mulchaey J. S., Bolte M., 2002, *ApJ*, **576**, 720
- Ko Y., et al., 2017, *ApJ*, **835**, 212
- Koopmans L. V. E., et al., 2009, *ApJ*, **703**, L51
- Kubo J. M., Stebbins A., Annis J., Dell’Antonio I. P., Lin H., Khiabani H., Frieman J. A., 2007, *ApJ*, **671**, 1466
- Lavaux G., Hudson M. J., 2011, *MNRAS*, **416**, 2840
- Loubser S. I., Sansom A. E., Sánchez-Blázquez P., Soechting I. K., Bromage G. E., 2008, *MNRAS*, **391**, 1009
- Ma C.-P., Greene J. E., McConnell N., Janish R., Blakeslee J. P., Thomas J., Murphy J. D., 2014, *ApJ*, **795**, 158
- Merritt D., Saha P., 1993, *ApJ*, **409**, 75
- Morganti L., Gerhard O., Coccato L., Martínez-Valpuesta I., Arnaboldi M., 2013, *MNRAS*, **431**, 3570
- Murphy J. D., Gebhardt K., Adams J. J., 2011, *ApJ*, **729**, 129
- Murphy J. D., Gebhardt K., Cradit M., 2014, *ApJ*, **785**, 143
- Napolitano N. R., et al., 2009, *MNRAS*, **393**, 329
- Newman A. B., Treu T., Ellis R. S., Sand D. J., Nipoti C., Richard J., Jullo E., 2013, *ApJ*, **765**, 24
- Newman A. B., Ellis R. S., Treu T., 2015, *ApJ*, **814**, 26
- Pandya V., et al., 2017, *ApJ*, **837**, 40
- Pota V., et al., 2013, *MNRAS*, **428**, 389
- Pota V., et al., 2015a, *MNRAS*, **450**, 1962
- Pota V., et al., 2015b, *MNRAS*, **450**, 3345
- Raskutti S., Greene J. E., Murphy J. D., 2014, *ApJ*, **786**, 23
- Richtler T., Salinas R., Misgeld I., Hilker M., Hau G. K. T., Romanowsky A. J., Schuberth Y., Spolaor M., 2011, *A&A*, **531**, A119
- Richtler T., Hilker M., Kumar B., Bassino L. P., Gómez M., Dirsch B., 2014, *A&A*, **569**, A41
- Rines K., Geller M. J., Kurtz M. J., Diaferio A., 2003, *AJ*, **126**, 2152
- Romanowsky A. J., Douglas N. G., Arnaboldi M., Kuijken K., Merrifield M. R., Napolitano N. R., Capaccioli M., Freeman K. C., 2003, *Science*, **301**, 1696
- Rubin V. C., Ford Jr. W. K., Thonnard N., 1980, *ApJ*, **238**, 471
- Schauer A. T. P., Remus R.-S., Burkert A., Johansson P. H., 2014, *ApJ*, **783**, L32
- Schindler S., Binggeli B., Böhringer H., 1999, *A&A*, **343**, 420
- Schuberth Y., Richtler T., Hilker M., Dirsch B., Bassino L. P., Romanowsky A. J., Infante L., 2010, *A&A*, **513**, A52
- Sembach K. R., Tonry J. L., 1996, *AJ*, **112**, 797
- Simien F., Prugniel P., 1997, *A&AS*, **126**
- Simien F., Prugniel P., 1998, *A&AS*, **131**, 287
- Simien F., Prugniel P., 2000, *A&AS*, **145**, 263
- Skibba R. A., van den Bosch F. C., Yang X., More S., Mo H., Fontanot F., 2011, *MNRAS*, **410**, 417
- Skrutskie M. F., et al., 2006, *AJ*, **131**, 1163
- Smith R. J., Lucey J. R., Edge A. C., 2017, *MNRAS*, **471**, 383
- Sonnenfeld A., Treu T., Gavazzi R., Suyu S. H., Marshall P. J., Auger M. W., Nipoti C., 2013, *ApJ*, **777**, 98
- Strader J., et al., 2011, *ApJS*, **197**, 33
- Thomas J., et al., 2007, *MNRAS*, **382**, 657
- Thomas J., et al., 2011, *MNRAS*, **415**, 545
- Thomas J., Saglia R. P., Bender R., Erwin P., Fabricius M., 2014, *ApJ*, **782**, 39
- Thomas J., Ma C.-P., McConnell N. J., Greene J. E., Blakeslee J. P., Janish R., 2016, *Nature*, **532**, 340
- Tonry J. L., 1985, *AJ*, **90**, 2431
- Treu T., Koopmans L. V., Bolton A. S., Burles S., Moustakas L. A., 2006, *ApJ*, **640**, 662
- Veale M., et al., 2017a, *MNRAS*, **464**, 356
- Veale M., Ma C.-P., Greene J. E., Thomas J., Blakeslee J. P., McConnell N., Walsh J. L., Ito J., 2017b, *MNRAS*, **471**, 1428
- Ventimiglia G., Gerhard O., Arnaboldi M., Coccato L., 2010, *A&A*, **520**, L9
- Verolme E. K., et al., 2002, *MNRAS*, **335**, 517
- Wilkinson A., Sharples R. M., Fosbury R. A. E., Wallace P. T., 1986, *MNRAS*, **218**, 297
- Wu X., Tremaine S., 2006, *ApJ*, **643**, 210

Wu X., Gerhard O., Naab T., Oser L., Martinez-Valpuesta I., Hilz
M., Churazov E., Lyskova N., 2014, *MNRAS*, **438**, 2701
Zhang H.-X., et al., 2015, *ApJ*, **802**, 30
van de Sande J., et al., 2017, *ApJ*, **835**, 104

APPENDIX A: INDIVIDUAL PROFILES

Each galaxy in our sample is fit to [Equation 1](#) as described in [Section 3.1](#). [Figure A1](#) shows the σ profiles for all 90 galaxies (in the same order as [Table 1](#)), with the best-fit profile overlaid in red.

This paper has been typeset from a $\text{T}_{\text{E}}\text{X}/\text{L}^{\text{A}}\text{T}_{\text{E}}\text{X}$ file prepared by the author.

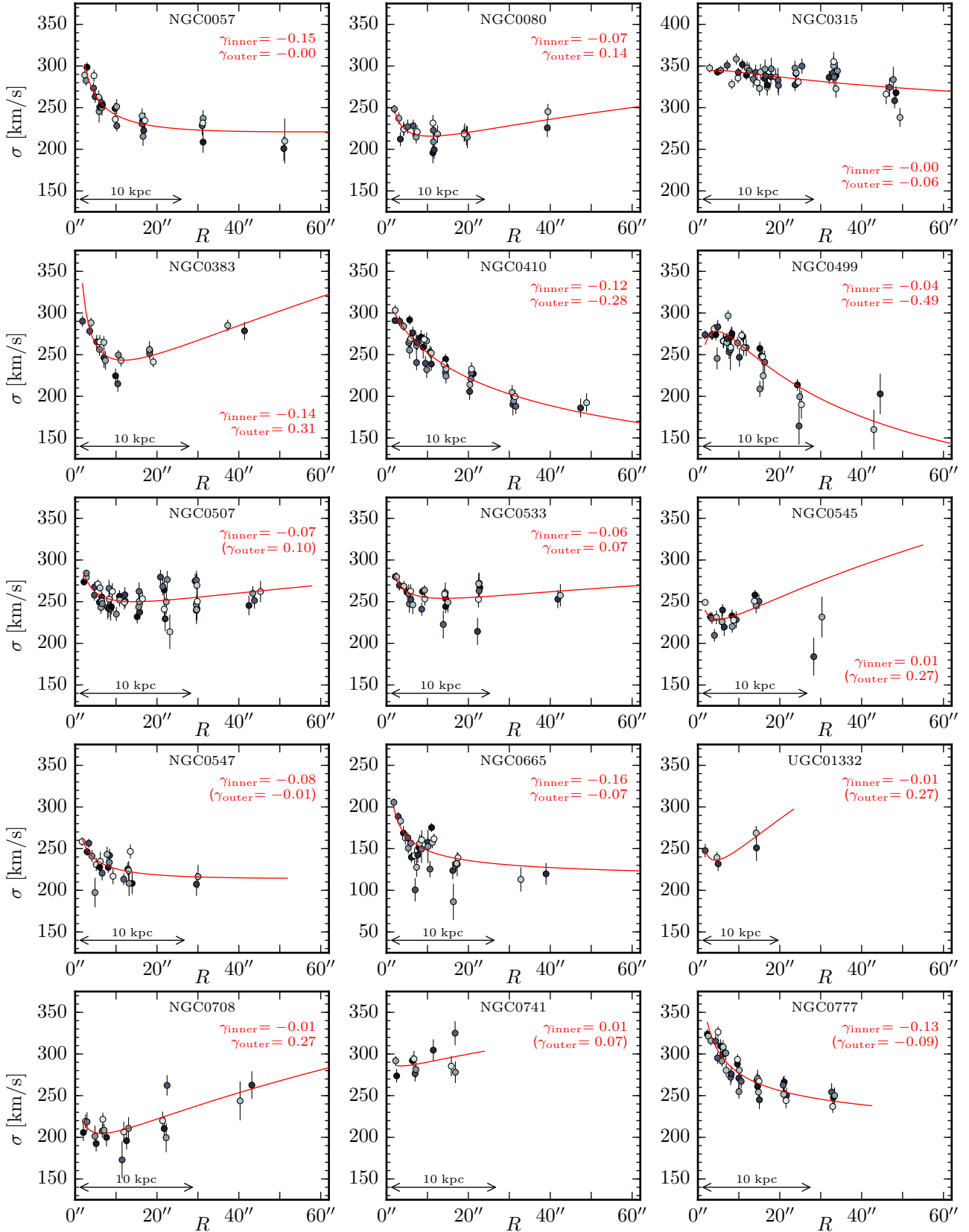


Figure A1. Individual galaxy dispersion profiles. Within each galaxy, σ for each spatial bin is shown with error bars, with point color corresponding to angle from major axis; black and white correspond to positive and negative major axis, and gray corresponds to the minor axis. Double power law fits are shown in red, with the local power law slope at 2 kpc (γ_{inner}) and 20 kpc (γ_{outer}) from [Table 1](#). If the maximum extent of the galaxy data is less than 20 kpc, the local slope at R_{max} is shown in parentheses.

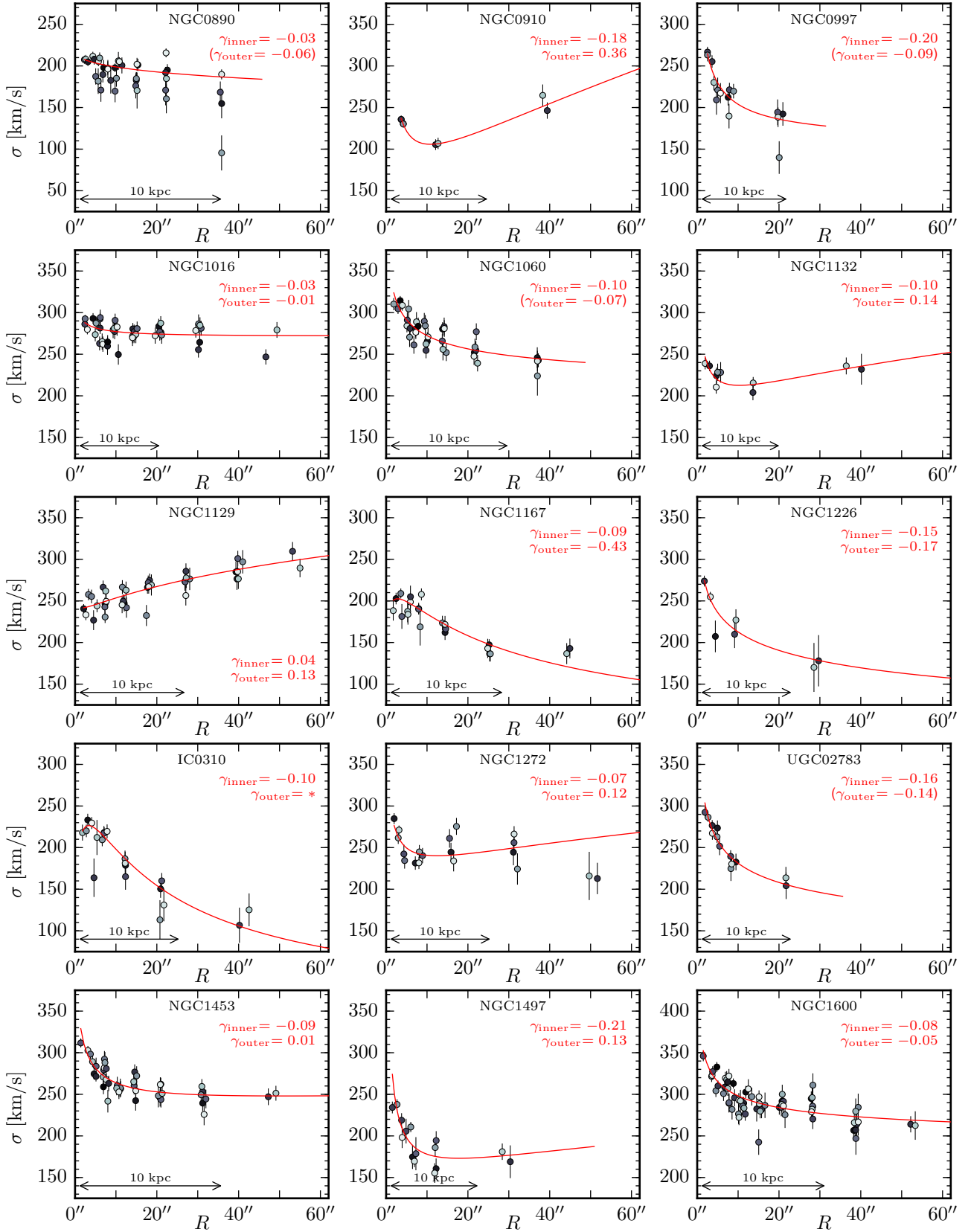


Figure A1. (continued)

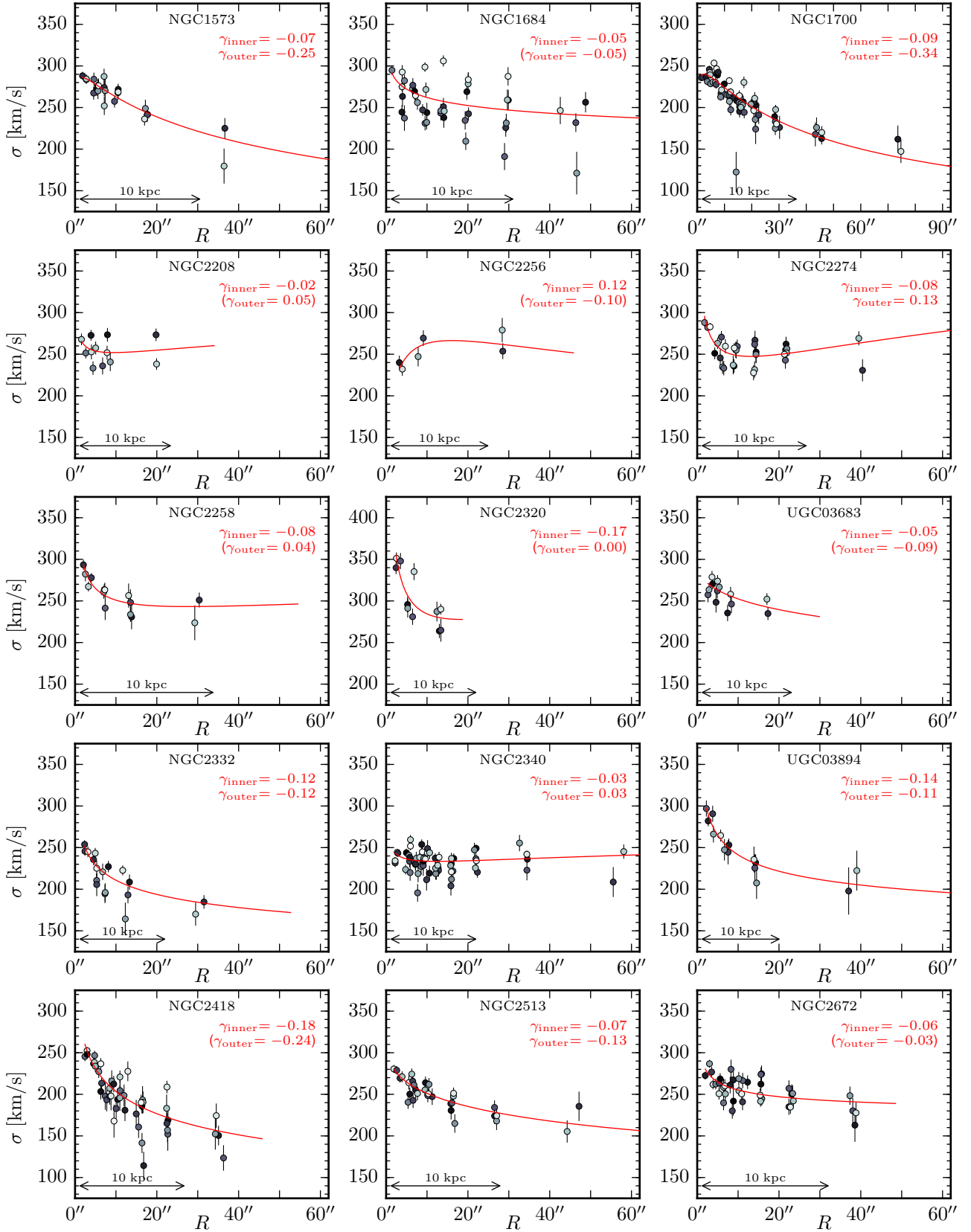


Figure A1. (continued)

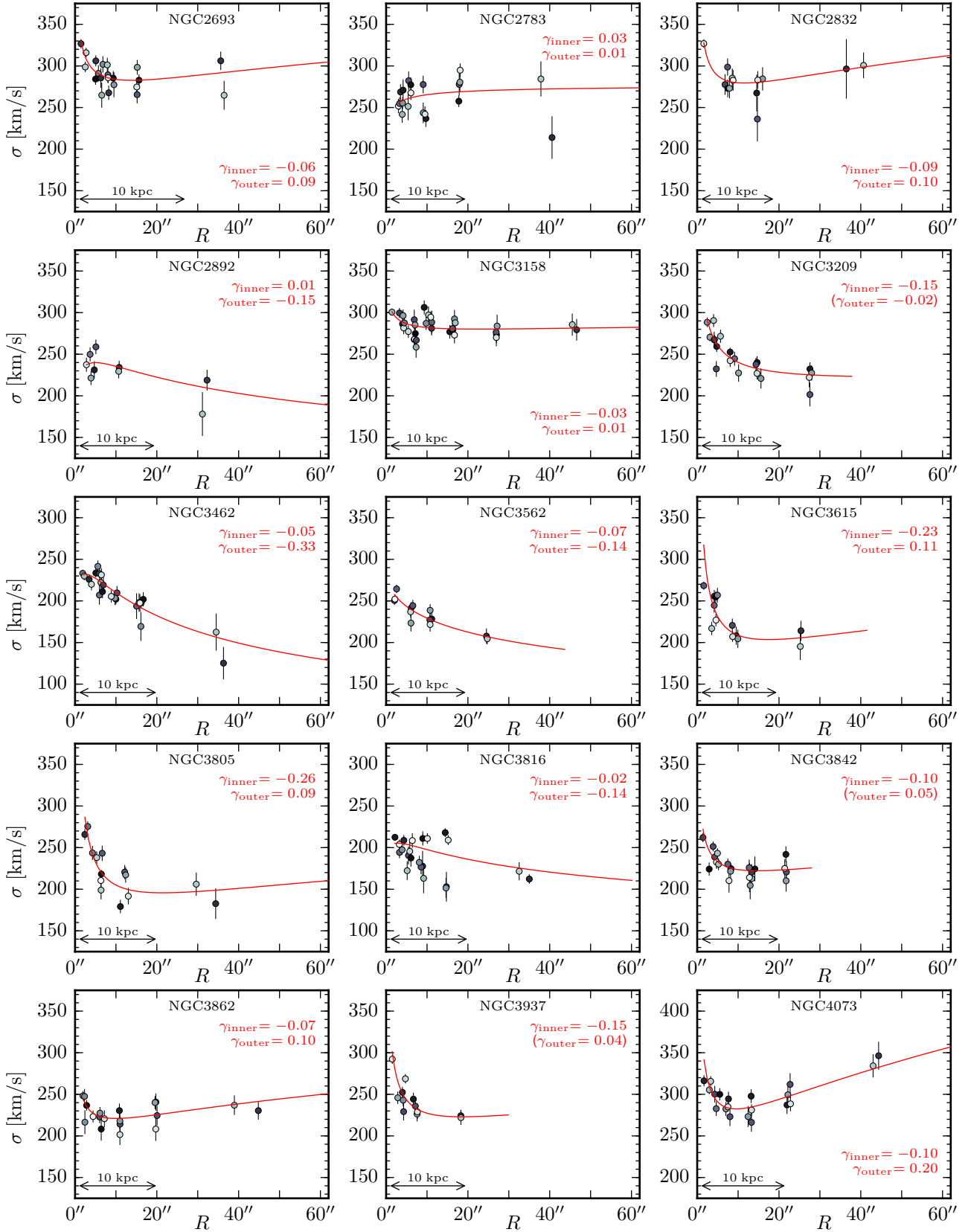


Figure A1. (continued)

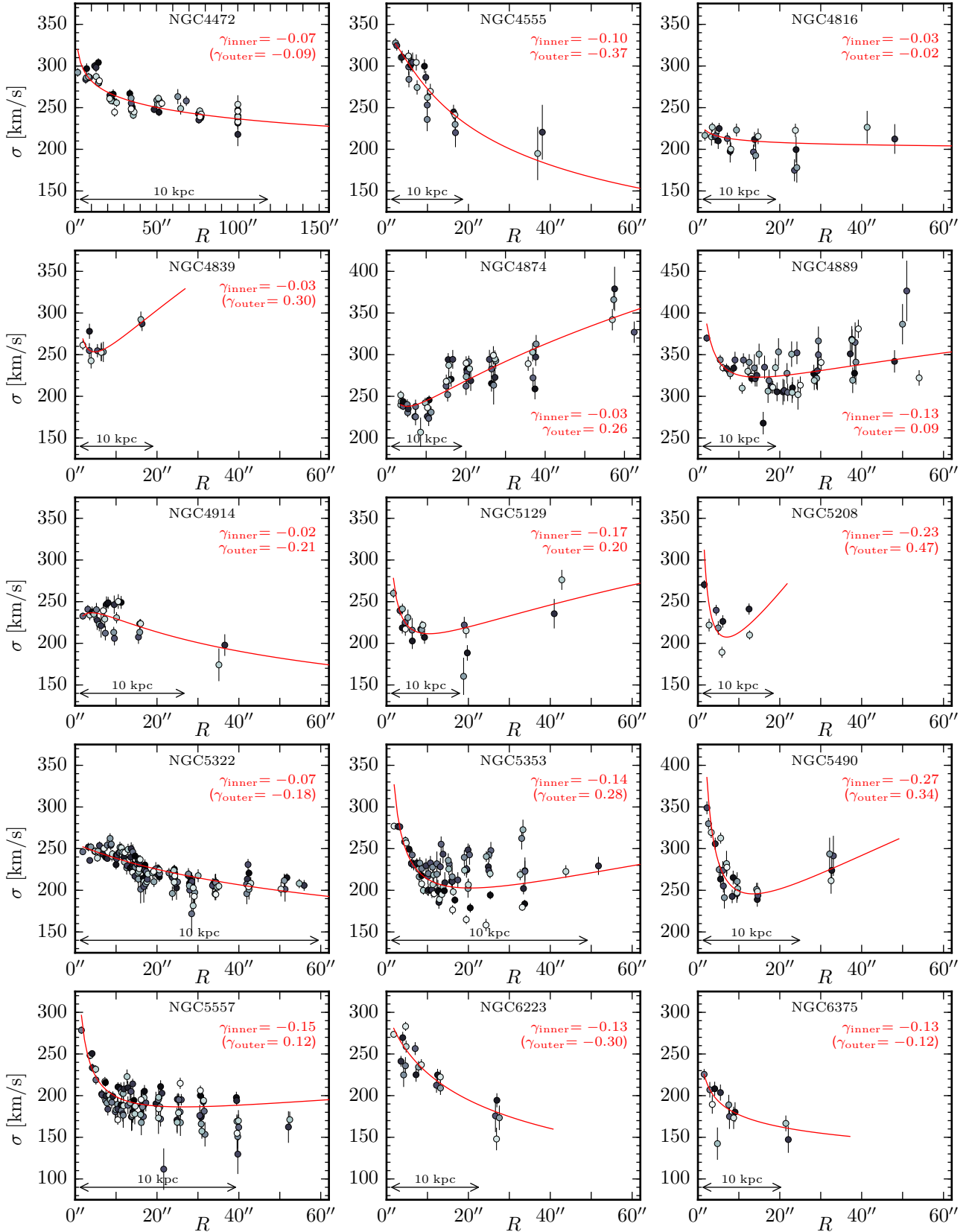


Figure A1. (continued)

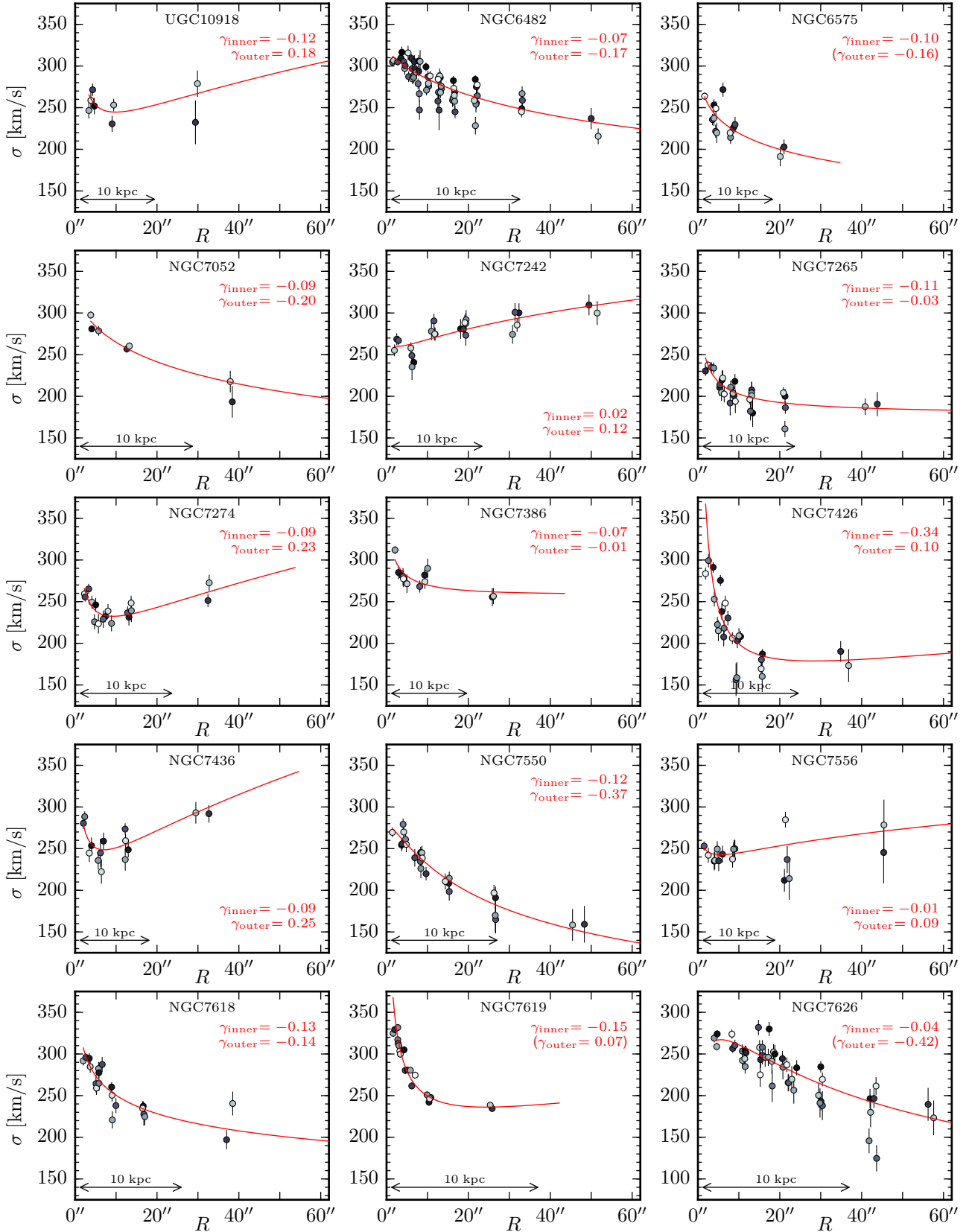


Figure A1. (continued)